Dynamics and transport properties of Kondo insulators

N S Vidhyadhiraja[1]**, Victoria E Smith**[1]**, David E Logan**[1,4] **and H R Krishnamurthy**[2,3]

[1] University of Oxford, Physical and Theoretical Chemistry Laboratory, South Parks Road, Oxford OX1 3QZ, UK
[2] Department of Physics, IISc, Bangalore 560 012, India
[3] JNCASR, Jakkur, Bangalore 506 064, India

E-mail: dlogan@physchem.ox.ac.uk

Abstract

A many-body theory of paramagnetic Kondo insulators is described, focusing specifically on single-particle dynamics, scattering rates, dc transport and optical conductivities. This is achieved by development of a non-perturbative local moment approach to the symmetric periodic Anderson model within the framework of dynamical mean-field theory. Our natural focus is the strong-coupling, Kondo lattice regime, in particular the resultant 'universal' scaling behaviour in terms of the single, exponentially small low-energy scale characteristic of the problem. Dynamics/transport on all relevant (ω, T)-scales are considered, from the gapped/activated behaviour characteristic of the low-temperature insulator through to explicit connection to single-impurity physics at high ω and/or T; and for optical conductivities emphasis is given to the nature of the optical gap, the temperature scale responsible for its destruction and the consequent clear distinction between indirect and direct gap scales. Using scaling, explicit comparison is also made to experimental results for dc transport and optical conductivities of $Ce_3Bi_4Pt_3$, SmB_6 and YbB_{12}. Good agreement is found, even quantitatively; and a mutually consistent picture of transport and optics results.

1. Introduction

In the field of strongly correlated electrons, lanthanide- or actinide-based heavy electron materials constitute a longstanding challenge to experimentalists and theorists alike [1, 2]. The majority of such systems, heavy fermions, are of course metallic, whether they be paramagnetic or ordered, Fermi- or non-Fermi liquids. Among them however resides a class of materials

[4] Author to whom any correspondence should be addressed.

with insulating ground states: the so-called Kondo insulators, containing a large variety of compounds (for reviews see e.g. [3–7]), and well known examples including $Ce_3Bi_4Pt_3$, SmB_6, YbB_{12}, CeRhAs and FeSi. This mainly cubic class of paramagnetic systems exhibits narrow-gap insulating/semiconducting behaviour at low temperatures, while their 'high'-temperature behaviour is largely indistinguishable from metallic heavy fermions, amounting in essence to a lattice of f ions that scatter conduction electrons independently via the Kondo effect. The insulating gap has long been argued (see e.g. [3]) to arise from hybridization between essentially localized f levels and a broad conduction band, the essential physics involving a flat f band crossing one conduction band such that there are exactly two electrons per unit cell ('half-filling'); albeit that the resultant hybridization gap is not of course a simple one-electron entity, being strongly renormalized by many-body interactions that reflect the localized and hence correlated nature of the f levels. As such, the Kondo insulators provide [3] a realization of the simplest, canonical model for understanding heavy electron systems [1, 2]: the half-filled periodic Anderson model (PAM), in which each lattice site contains a non-degenerate, correlated f level hybridizing locally with a non-interacting conduction band, and which represents the natural lattice generalization of the Anderson impurity model (AIM) [2].

In the present paper we consider the half-filled, symmetric PAM within the powerful framework of dynamical mean-field theory (DMFT, reviewed in [8–11]). Formally exact in the large-dimensional limit, DMFT provides a tangible approximation in finite dimensions, whereby electron dynamics become essentially local but remain wholly non-trivial [8–11]. Our basic aims here are to provide a many-body description of dynamical and transport properties of paramagnetic Kondo insulators, specifically single-particle dynamics, dynamical conductivities and static electrical transport; and to develop the theory to the point where quantitative comparison with experiment can be made.

These goals are of course easier stated than achieved, and the PAM has been studied extensively within DMFT via a wide range of techniques. Numerical methods include the numerical renormalization group (NRG) [12, 13], quantum Monte Carlo (QMC) [14–17] and exact diagonalization [18], while theoretical approaches include perturbation theory in the interaction strength [19, 20], iterated perturbation theory (IPT) [21, 22], the lattice non-crossing approximation [23, 24] and the simpler average *t*-matrix approximation [25], large-*N* mean-field theory [26, 27] and the Gutzwiller approach [28, 29]. NRG aside, however, the above techniques suffer in general from well recognized limitations: whether it be an inability to handle large interactions and hence recover the exponentially small scales that are the hallmark of strongly correlated systems, failure to recover Fermi liquid behaviour at low energies, unrealistic confinement to the lowest energies and so on. Within DMFT all correlated lattice-fermion models reduce to an effective quantum impurity hybridizing self-consistently with the surrounding fermionic bath [8–11], i.e. to an effective, self-consistent AIM. Techniques for the latter thus underpin the former. Motivated in part by this we have been developing a 'local moment approach' (LMA) to quantum impurity models (AIMs) [30–35], the main emphasis of which is on dynamics and transport. Intrinsically non-perturbative and able to capture the spin-fluctuation physics characteristic of the strongly correlated Kondo regime, the LMA encompasses all interaction strengths U and recovers simple perturbative behaviour in weak coupling [30]. Dynamics on all energy scales are handled, and the low-energy dictates of Fermi liquid behaviour satisfied (although the approach is not confined to Fermi liquid ground states, see e.g. [33, 34]). Results for dynamics arising from the LMA have been shown [30–32, 34] to give very good agreement with NRG calculations; and, for static magnetic properties, with exact results from the Bethe ansatz [35].

In a recent paper [36] we have further developed the LMA to encompass $T = 0$ single-particle dynamics/spectra of the symmetric PAM. While plain perturbative behaviour is again

recovered in weak coupling, the natural focus of [36] was on the strong-coupling (i.e. large-U) Kondo lattice regime. At sufficiently low energies in the vicinity of the Fermi level, the LMA recovers correctly the 'insulating Fermi liquid' behaviour [36] that reflects adiabatic continuity in U to the non-interacting limit of the simple hybridization-gap insulator [2, 10]. This is manifest in preservation of the single-particle gap, now characterized by a renormalized gap scale Δ_g which is reduced from its non-interacting counterpart by the quasiparticle weight Z that embodies many-body interactions. In agreement with consensus [12–15, 24, 28, 29], strong-coupling dynamics were found [36] to be characterized by the *single* low-energy gap scale Δ_g, which is exponentially small in strong coupling [36] (reflecting its dependence on Z), thus leading to a clear separation between low- and high-energy scales. In consequence, 'low'-ω dynamics exhibit scaling: being dependent solely and universally upon ω/Δ_g, with *no* dependence on the 'bare' high-energy parameters (U etc) that enter the PAM Hamiltonian. The simplest manifestation of scaling is that at sufficiently low energies ω/Δ_g the spectral behaviour amounts [2, 10] to a quasiparticle renormalization of the non-interacting hybridization-gap insulator, which is of course the justification for renormalized band structure ideas. By itself, however, such quasiparticle behaviour gives rather a crude caricature of the scaling spectra, for it is confined to the immediate vicinity of the Fermi level $\omega = 0$ [36]; beyond which, and on scales on the order of Δ_g itself, non-trivial dynamics rapidly sets in, embodied in long, slowly varying spectral tails that reflect genuine many-body scattering/lifetime effects. As we show in the present paper, it is in fact this that dominates both dynamics and transport properties for *all* temperatures.

The paper is organized as follows. The model and basic underlying theory are discussed in section 2, formulated for an arbitrary host lattice, and including relevant aspects of the LMA in general (section 2.1) as well as the specific class of diagrams contributing to the associated dynamical self-energies $\Sigma_\sigma(\omega; T)$ that we employ here in practice. Section 3 deals briefly with some basic formal results for conduction electron scattering rates, electrical transport and optical conductivities. Here and hereafter we consider explicitly and together two canonical host lattices [8–11], the hypercubic and Bethe lattices (BL); our aim throughout being to emphasize both the differences and, more importantly, similarities between these two representative cases. Results arising from the LMA are then presented systematically in sections 4. Our primary emphasis is again the strong-coupling Kondo lattice regime of the PAM, this being both where the theoretical difficulties lie and the regime generally applicable to small-gap Kondo insulators. By the same token we focus largely, albeit not exclusively, on the scaling behaviour of dynamics and/or transport, now depending universally on $\tilde{\omega} = \omega/\Delta_g$ *and* $\tilde{T} = T/\Delta_g$. This is important for many reasons, not least because the lack of scale separation inherent to some previous approaches has we believe led to a number of misconceptions in the literature, particularly in regard to the scales relevant to the T- and ω-dependence of the conductivity. In sections 4 and 5, and considering *all* $\tilde{\omega}$ and $\tilde{T}$ scales, single-particle dynamics, conduction electron scattering rates and dc transport are considered, including explicit connection to single-impurity physics at high frequencies and/or temperatures ('Kondo logs' etc). Optical conductivities $\sigma(\omega; T)$ are considered in section 6, with particular emphasis given to the nature of the optical gap and the clear separation between indirect and direct gap scales in both the ω-dependence and thermal evolution of $\sigma(\omega; T)$.

In section 7 we turn to experiment, considering three prototypical materials for which extensive and reliable data are available [3–7], namely $Ce_3Bi_4Pt_3$, SmB_6 and YbB_{12}: our aim being direct comparison between the present theory and experimental results for both dc transport and optical conductivities. That may be achieved in a minimalist fashion, employing directly the scaling behaviour discussed in sections 4–6, which requires neither multiparameter fits nor in general a specification of the bare model parameters. Good agreement between theory

and experiment is found, even quantitatively, with many of the characteristic features arising theoretically being directly apparent in experiment, and a mutually consistent description of transport and optics thereby arising. The paper concludes with a brief summary.

2. Model and theory

In standard notation, the Hamiltonian for the PAM is given by

$$\hat{H} = -t \sum_{(i,j),\sigma} c_{i\sigma}^{\dagger} c_{j\sigma} + \sum_{i,\sigma} \left(\epsilon_f + \frac{U}{2} f_{i-\sigma}^{\dagger} f_{i-\sigma} \right) f_{i\sigma}^{\dagger} f_{i\sigma} + V \sum_{i,\sigma} (f_{i\sigma}^{\dagger} c_{i\sigma} + \text{h.c.}) \tag{2.1}$$

The first term describes the uncorrelated conduction (c) band with nearest-neighbour hopping $t_{ij} = t$, rescaled as $t \propto t_*/\sqrt{Z_c}$ in the large-dimensional limit where the coordination number $Z_c \to \infty$ [8–11] (with t_* the basic unit of energy). The second term refers to the f levels with site energies ϵ_f and on-site repulsion U, such that $\epsilon_f = -\frac{U}{2}$ for the particle–hole (p–h) symmetric PAM considered here, for which $n_f = \sum_{\sigma} \langle f_{i\sigma}^{\dagger} f_{i\sigma} \rangle = 1$ and $n_c = \sum_{\sigma} \langle c_{i\sigma}^{\dagger} c_{i\sigma} \rangle = 1$ (for all U) as appropriate to the Kondo insulating state. The final term in equation (2.1) describes c/f-level hybridization via the local matrix element V, whence the model is characterized by two independent dimensionless parameters, namely U/t_* and V/t_*.

Our natural focus is on local single-particle dynamics, embodied in the retarded Green functions $G_{ii}^f(\omega)$ ($\leftrightarrow -i\theta(t)\langle\{f_{i\sigma}(t), f_{i\sigma}^{\dagger}\}\rangle$) and likewise $G_{ii}^c(\omega)$ for the c levels, with corresponding local spectra $D_{ii}^{\nu}(\omega) = -\frac{1}{\pi} \text{Im } G_{ii}^{\nu}(\omega)$ (and ν = c or f). A knowledge of local dynamics and their thermal evolution is in turn sufficient within DMFT [8–11] to determine optical and transport properties, as detailed in section 3.

We begin with some brief remarks on the trivial limit $V = 0$, where (equation (2.1)) the f levels decouple from the free conduction band. The latter is specified by its local density of states $\rho_0(\epsilon) = -\frac{1}{\pi} \text{Im } g_0(\epsilon)$, and it proves useful in the following to denote by $\text{H}(z)$ the Hilbert transform

$$\text{H}(z) = \int_{-\infty}^{\infty} d\epsilon \, \frac{\rho_0(\epsilon)}{z - \epsilon} \tag{2.2}$$

for arbitrary complex z. The free c-electron (local) propagator $g_0(\omega)$ is itself given simply by

$$g_0(\omega) = \text{H}(\omega^+) \tag{2.3a}$$
$$= [\omega^+ - S_0(\omega)]^{-1} \tag{2.3b}$$

with $\omega^+ = \omega + i0^+$ here and throughout; where (as used below) equation (2.3b) defines the Feenberg self-energy $S_0(\omega)$ [37, 38], with $S_0(\omega) \equiv S[g_0]$ a functional of g_0 (since $g_0 = \text{H}(S + 1/g_0)$). While our subsequent discussion holds for an arbitrary conduction band $\rho_0(\epsilon)$, specific results will be given in section 4 for the BL and hypercubic lattice (HCL), for which within DMFT the $\rho_0(\epsilon)$ are respectively a semi-ellipse and an unbounded Gaussian, given explicitly by [8–11]:

$$\rho_0(\epsilon) = \begin{cases} \dfrac{2}{\pi t_*} [1 - (\epsilon/t_*)^2]^{\frac{1}{2}}: & |\epsilon| \leqslant t_* \qquad \text{BL} \\[3mm] \dfrac{1}{\sqrt{\pi} t_*} \exp(-[\epsilon/t_*]^2) & \text{HCL.} \end{cases} \tag{2.4}$$

As noted in section 1 we are interested in the homogeneous paramagnetic phase of the PAM, for which the $G_{ii}^{\nu}(\omega) \equiv G^{\nu}(\omega)$ are site independent. The major simplifying feature of DMFT is that the f-electron self-energy is site diagonal [8–11], and from straightforward

application of Feenberg renormalized perturbation theory [37, 38] the $G^{\nu}(\omega)$ are given by

$$G^c(\omega) = \left[\omega^+ - \frac{V^2}{\omega^+ - \Sigma_f(\omega; T)} - S(\omega)\right]^{-1} \qquad (2.5a)$$

$$G^f(\omega) = \left[\omega^+ - \Sigma_f(\omega; T) - \frac{V^2}{\omega^+ - S(\omega)}\right]^{-1}. \qquad (2.5b)$$

Here $\Sigma_f(\omega; T)$ is the conventional single self-energy (defined to exclude the trivial Hartree contribution which identically cancels $\epsilon_f = -\frac{U}{2}$), such that $\Sigma_f(\omega; T) = \Sigma_f^R(\omega; T) - i\Sigma_f^I(\omega; T)$ with $\Sigma_f^I(\omega; T) \geqslant 0$ for all (ω, T), and with p–h symmetry reflected in

$$\Sigma_f(\omega; T) = -[\Sigma_f(-\omega; T)]^* \qquad (2.6)$$

together with $S(\omega) = -[S(-\omega)]^*$, $G^{\nu}(\omega) = -[G^{\nu}(-\omega)]^*$ and hence $D^{\nu}(\omega) = D^{\nu}(-\omega)$ for the spectra. Equation (2.5b) embodies the connection to an effective impurity model that is inherent to DMFT [8–11], for it may be cast in the 'single-impurity' form $G^f(\omega) = [\omega^+ - \Sigma_f(\omega; T) - \Delta_{eff}(\omega)]^{-1}$; with an effective hybridization $\Delta_{eff}(\omega) = V^2[\omega^+ - S(\omega)]^{-1}$ which, in contrast to that for a pure AIM and by virtue of its dependence on the Feenberg self-energy $S(\omega)$, depends implicitly on coupling to the other sites in the correlated lattice and as such must thus be self-consistently determined. Specifically, the Feenberg self-energy $S(\omega) \equiv S[G^c]$ is precisely the same functional of $G^c(\omega)$ as it is of $g_0(\omega)$ in the $V = 0$ limit (e.g. $S = \frac{1}{4}t_*^2 G^c$ for the BL). In consequence, G^c is given using equation (2.5a) by

$$G^c(\omega) = H(\gamma) \qquad (2.7)$$

where

$$\gamma(\omega) = \omega^+ - \frac{V^2}{\omega^+ - \Sigma_f(\omega; T)} \qquad (2.8)$$

(and we add in passing that in physical terms $\gamma_I(\omega) = \operatorname{Im} \gamma(\omega)$ gives the conduction electron scattering rate which will be considered further in section 3).

It is this that, for an arbitrary $\rho_0(\epsilon)$, prescribes the conventional 'single-self-energy' route to the propagators $G^{\nu}(\omega)$: given $\Sigma_f(\omega; T)$, and hence $\gamma(\omega)$, $G^c(\omega) = H(\gamma)$ follows directly by Hilbert transformation; $S(\omega)$ follows (from equation (2.5a)) as

$$S(\omega) = \gamma - \frac{1}{H(\gamma)} \qquad (2.9)$$

and $G^f(\omega)$ then follows in turn from equation (2.5b). In practice of course the problem must be solved iteratively and self-consistently, because the approximate $\Sigma_f(\omega; T)$ employed will itself in general be a functional of self-consistently determined propagators. Self-consistent second-order perturbation theory in U [20] provides a direct example, as too does IPT [21] where $\Sigma_f(\omega; T)$ is constructed from the second-order (in U) skeleton diagram, employing host/medium f-electron propagators $\mathcal{G}(\omega) = [(G^f(\omega))^{-1} + \Sigma_f(\omega; T)]^{-1}$ given from equation (2.5b) by

$$\mathcal{G}(\omega) = \left[\omega^+ - \frac{V^2}{\omega^+ - S(\omega)}\right]^{-1} \qquad (2.10)$$

and thus dependent on $S(\omega)$ itself. Results arising from IPT will be discussed in sections 4–6.

2.1. Local moment approach

In the conventional route to dynamics sketched above, the success of any particular theory is naturally determined by the approximation employed for the single self-energy Σ_f. Therein lie

well known difficulties [2], notably the inability of conventional perturbation theory to handle strong interactions in general, and to recover exponentially small scales that are the hallmark of strongly correlated behaviour, together with the divergences that plague perturbation theory in U [2] if one attempts to perform essentially standard diagrammatic resummations (e.g. RPA) of the sort one intuitively expects should be required to capture the regime of strong electron correlations. For these reasons the LMA [30–36] eschews an approach based directly on the single Σ_f, and focuses instead on a two-self-energy description that is a natural consequence of the mean-field approach from which it starts.

There are three essential elements to the LMA.

 (i) First that f-electron local moments ('μ'), viewed as the initial effect of interactions, are introduced explicitly from the outset. The starting point is thus broken symmetry static mean-field (MF, i.e. unrestricted Hartree–Fock); containing two degenerate, local symmetry broken MF states, corresponding to $\mu = \pm|\mu|$. Grossly deficient by itself (see [36]), MF nevertheless provides a starting point for a non-perturbative many-body approach, to which end

 (ii) the LMA employs the two-self-energy description that is a natural consequence of the underlying two local saddle points. The associated self-energies are built diagrammatically from the underlying MF propagators, and include in particular a non-perturbative class of diagrams (section 2.2 and figure 1 below) that capture the spin-flip dynamics essential to describe the strongly correlated regime.

(iii) The final key idea behind the LMA at $T = 0$ is that of symmetry restoration (SR) [30–36]: self-consistent restoration of the broken symmetry endemic at pure MF level, and hence recovery on the lowest energy scales of the Fermi liquid/quasiparticle behaviour that reflects adiabatic continuity in U to the non-interacting limit.

As detailed in [36] the $G^\nu(\omega)$, which are as they must be rotationally invariant, are expressed formally as (cf equations (2.5))

$$G^\nu(\omega) = \tfrac{1}{2}[G^\nu_\uparrow(\omega) + G^\nu_\downarrow(\omega)] \tag{2.11}$$

where

$$G^c_\sigma(\omega) = \left[\omega^+ - \frac{V^2}{\omega^+ - \tilde{\Sigma}_\sigma(\omega; T)} - S(\omega)\right]^{-1} \tag{2.12a}$$

$$G^f_\sigma(\omega) = \left[\omega^+ - \tilde{\Sigma}_\sigma(\omega; T) - \frac{V^2}{\omega^+ - S(\omega)}\right]^{-1} \tag{2.12b}$$

(and $\sigma = \uparrow/\downarrow$ or $+/-$), with the f-electron self-energies separated as

$$\tilde{\Sigma}_\sigma(\omega; T) = -\frac{\sigma}{2}U|\bar{\mu}| + \Sigma_\sigma(\omega; T). \tag{2.13}$$

The first term here represents the purely static Fock bubble diagram that alone is retained at pure MF level (with $|\bar{\mu}|$ given explicitly by equation (2.17) below). The second term $\Sigma_\sigma(\omega; T) = \Sigma^R_\sigma(\omega; T) - i\Sigma^I_\sigma(\omega; T)$, is the all-important dynamical contribution mentioned above, with p–h symmetry reflected in

$$\Sigma_\sigma(\omega; T) = -[\Sigma_{-\sigma}(-\omega; T)]^* \tag{2.14}$$

(such that $G^\nu_\sigma(\omega) = -[G^\nu_{-\sigma}(-\omega)]^*$ and hence $G^\nu(\omega) = -[G^\nu(-\omega)]^*$).

Equations (2.11) and (2.12) are the two-self-energy counterparts of the single-self-energy equations (2.5). For an arbitrary conduction band $\rho_0(\epsilon)$ and given $\{\tilde{\Sigma}_\sigma(\omega; T)\}$, they

may likewise be solved straightforwardly (cf the above discussion of equations (2.7)–(2.9)): defining

$$\tilde{\gamma}_\sigma(\omega) = \omega^+ - \frac{V^2}{\omega^+ - \tilde{\Sigma}_\sigma(\omega; T)} \tag{2.15}$$

such that $G^c(\omega) = \frac{1}{2}\sum_\sigma [\tilde{\gamma}_\sigma - S]^{-1}$ (equations (2.11) and (2.12a)), and comparing to $G^c(\omega) = [\gamma - S]^{-1}$ (equations (2.5a) and (2.8)), the $\tilde{\gamma}_\sigma$'s are related to the single $\gamma(\omega)$ (equation (2.8)) by

$$\gamma(\omega) = \frac{1}{2}[\tilde{\gamma}_\uparrow(\omega) + \tilde{\gamma}_\downarrow(\omega)] + \frac{[\frac{1}{2}(\tilde{\gamma}_\uparrow(\omega) - \tilde{\gamma}_\downarrow(\omega))]^2}{S(\omega) - \frac{1}{2}[\tilde{\gamma}_\uparrow(\omega) + \tilde{\gamma}_\downarrow(\omega)]}. \tag{2.16}$$

Given $\tilde{\Sigma}_\sigma(\omega; T)$ and hence $\tilde{\gamma}_\sigma(\omega)$, this equation together with $S(\omega) = \gamma - 1/H(\gamma)$ (equation (2.9)) may be solved iteratively for $S(\omega)$ (employing an initial 'start-up' S, say $S = \frac{1}{4}t_*^2 g_0(\omega)$), which procedure is both straightforward and numerically fast. With $S(\omega)$ then known the $G^v(\omega)$ follow directly from equations (2.11) and (2.12). In particular, the underlying MF propagators may be obtained from this procedure in one shot, the static MF self-energies being given by $\tilde{\Sigma}_\sigma \equiv \tilde{\Sigma}_\sigma^0 = -\sigma x$ with $x = \frac{1}{2}U|\mu|$. For any given x, the MF propagators $g_\sigma^v(\omega)$ and hence spectra $d_\sigma^v(\omega) \equiv d_\sigma^v(\omega; x)$ thus follow; and at pure MF level the local moment $|\mu|$ is then found from solution of $|\mu| = |\bar{\mu}|$, where the Fock bubble $|\bar{\mu}| \equiv |\bar{\mu}(x)|$ appearing generally in equation (2.13) is given by

$$|\bar{\mu}| = \int_{-\infty}^{\infty} d\omega\, [d_\uparrow^f(\omega) - d_\downarrow^f(\omega)] f(\omega; T) \tag{2.17}$$

with $f(\omega; T) = [e^{\omega/T} + 1]^{-1}$ the Fermi function.

The single self-energy $\Sigma_f(\omega; T)$ likewise follows as a by-product of the above procedure, since solution of equations (2.9) and (2.16) given $\{\tilde{\Sigma}_\sigma(\omega; T)\}$ determines both $S(\omega)$ *and* $\gamma(\omega)$; whence (see equation (2.8)) $\Sigma_f(\omega; T) = \omega^+ - V^2[\omega^+ - \gamma(\omega)]^{-1}$ thus follows, which relation may be recast equivalently as

$$\Sigma_f(\omega; T) = \frac{1}{2}[\tilde{\Sigma}_\uparrow(\omega; T) + \tilde{\Sigma}_\downarrow(\omega; T)] + \frac{[\frac{1}{2}(\tilde{\Sigma}_\uparrow(\omega; T) - \tilde{\Sigma}_\downarrow(\omega; T))]^2}{\mathcal{G}^{-1}(\omega) - \frac{1}{2}[\tilde{\Sigma}_\uparrow(\omega; T) + \tilde{\Sigma}_\downarrow(\omega; T)]} \tag{2.18}$$

where $\mathcal{G}(\omega) = [\omega^+ - V^2(\omega^+ - S(\omega))^{-1}]^{-1}$ is precisely the host/medium f-propagator equation (2.10). The resultant conventional single self-energy may thus be obtained directly, given the two self-energies $\tilde{\Sigma}_\sigma(\omega; T)$ equation (2.13) (although not of course vice versa); and the particular class of diagrams contributing to the dynamical $\Sigma_\sigma(\omega; T)$ that we retain in practice are specified in section 2.2.

As mentioned above and discussed further in [36], the final, central idea behind the $T = 0$ LMA is self-consistent restoration of the broken symmetry inherent at MF level. This is embodied mathematically in the SR condition $\tilde{\Sigma}_\uparrow(\omega = 0; T = 0) = \tilde{\Sigma}_\downarrow(\omega = 0; T = 0)$ at the Fermi level $\omega = 0$; and hence $\tilde{\Sigma}_\sigma(0; 0) = 0$ (for either σ) for the p–h symmetric PAM here considered, i.e.

$$\tilde{\Sigma}_\uparrow^R(0; 0) = \Sigma_\uparrow^R(0; 0) - \frac{1}{2}U|\bar{\mu}| = 0 \tag{2.19}$$

(using $\tilde{\Sigma}_\sigma(0; 0) = \tilde{\Sigma}_\sigma^R(0; 0)$). In physical terms, satisfaction of SR ensures [36] that single-particle dynamics on the lowest energy scales amount to a quasiparticle renormalization of the non-interacting limit $U = 0$, reflecting Fermi liquid behaviour in the general sense of adiabatic continuity to that limit. For $U = 0$ ($= \Sigma_f$) the non-interacting Green functions are denoted by $g_0^v(\omega; V^2)$, with spectra $d_0^v(\omega; V^2)$ and the V^2-dependence explicit; such that

(via equations (2.2), (2.3a), (2.3b), (2.5), (2.7) and (2.8)) $d_0^c(\omega; V^2) = \rho_0(\omega - V^2/\omega)$ and $d_0^f(\omega; V^2) = \frac{V^2}{\omega^2} d_0^c(\omega; V^2)$ with $\rho_0(\epsilon)$ the free ($V = 0$) conduction band density of states, e.g. equations (2.4). For $U = 0$ and all $V \neq 0$ the system is thus of course a simple hybridization gap insulator [39], with a gap $\Delta_g^0(V^2)$ that is hard for the generic case of a bounded $\rho_0(\epsilon)$ (e.g. the BL, equation (2.4)) and (strictly) soft for an unbounded $\rho_0(\epsilon)$ satisfying $\rho_0(\epsilon) \to 0$ as $|\epsilon| \to \infty$ (e.g. the Gaussian characteristic of the HCL, equation (2.4)). If the SR condition equation (2.19) is satisfied then (see [36]) for $U > 0$ the leading, lowest-ω behaviour of the full $T = 0$ $G^\nu(\omega)$ follows as

$$G^c(\omega) \sim g_0^c(\omega; ZV^2) \tag{2.20a}$$

$$G^f(\omega) \sim Z g_0^f(\omega; ZV^2) \tag{2.20b}$$

where $Z = [1 - (\partial \Sigma^R(\omega; 0)/\partial \omega)_{\omega=0}]^{-1}$ is the quasiparticle weight (given equivalently by [36] $Z = [1 - (\partial \tilde{\Sigma}_\sigma^R(\omega; 0)/\partial \omega)_{\omega=0}]^{-1})$; resulting in preservation of the insulating gap, $\Delta_g = \Delta_g^0(ZV^2)$, that is generically reduced from the non-interacting hybridization gap by the quasiparticle weight factor Z, with $Z \ll 1$ in strong coupling.

Equations (2.20) embody the quasiparticle behaviour of the PAM on the lowest energy scales, i.e. the 'insulating Fermi liquid' behaviour that evolves continuously from the non-interacting limit. Imposition of SR equation (2.19), as a single condition *at* the Fermi level $\omega = 0$, naturally underlies the LMA, and amounts in practice, as detailed in [36], to a self-consistent determination of the local moment $|\mu|$ (superseding the pure MF condition $|\mu| = |\bar{\mu}(x)|$, see equation (2.17)).

2.2. Dynamical self-energies

Our final task is to specify the class of diagrams retained in practice for the dynamical $\Sigma_\sigma(\omega; T)$ (equation (2.13)). These embody self-consistent dynamical coupling of single-particle excitations to low-energy transverse spin fluctuations and are precisely as considered in [36] for $T = 0$, extended to finite T following arguments identical to [32] for the AIM; the reader is thus referred to [32, 36], for full details. The diagrams are summarized in figure 1 where wavy lines denote the local interaction U, the double-line propagator denotes the broken symmetry host/medium f-electron propagator $\tilde{\mathcal{G}}_{-\sigma}(\omega)$ specified below (equation (2.21)) and the local f-level transverse spin polarization propagator is shown as hatched; diagrammatic expansion of the resultant Σ_σ in terms of MF propagators and dynamical self-energy insertions is discussed in [36, 40].

In physical terms the diagrams shown in figure 1 describe correlated spin-flip scattering processes that are essential to capture in particular the strong-coupling Kondo lattice regime of the model; in which having, say, added a σ-spin electron to a $-\sigma$-spin occupied f level on site i, the $-\sigma$-spin hops off the f level thus generating an on-site spin flip (embodied in the transverse spin polarization propagator); the $-\sigma$-spin electron then propagates through the lattice/host in a correlated fashion, interacting *fully* with f electrons on *any* site $j \neq i$ (reflected in the host/medium $\tilde{\mathcal{G}}_{-\sigma}(\omega)$), before returning to site i at a later time whereupon the originally added σ-spin is removed (and which process simultaneously restores the spin flip on site i).

The renormalized medium f propagator $\tilde{\mathcal{G}}_{-\sigma}(\omega)$, which embodies correlated propagation of the $-\sigma$-spin electron through the lattice, is given explicitly by [36] (cf equation (2.10))

$$\tilde{\mathcal{G}}_{-\sigma}(\omega) = \left[\omega^+ - \frac{\sigma}{2}U|\mu| - \frac{V^2}{\omega^+ - S(\omega)}\right]^{-1}. \tag{2.21}$$
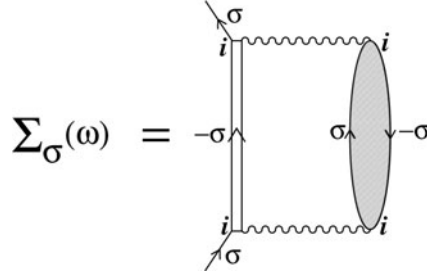
Figure 1. Class of diagrams for the f-electron self-energies $\Sigma_\sigma(\omega)$ here retained in practice. The interaction U is denoted by a wavy line and the renormalized host/medium propagator (see text) by a double line; the transverse spin polarization propagator is shown hatched.

As used below, $\tilde{\mathcal{G}}_\sigma(\omega)$ may be separated as $\tilde{\mathcal{G}}_\sigma(\omega) = \tilde{\mathcal{G}}_\sigma^+(\omega) + \tilde{\mathcal{G}}_\sigma^-(\omega)$ into the one-sided retarded Hilbert transforms, given by

$$\tilde{\mathcal{G}}_\sigma^\pm(\omega) = \int_{-\infty}^\infty d\omega_1 \frac{\tilde{\mathcal{D}}_\sigma(\omega_1)\theta(\pm\omega_1)}{\omega - \omega_1 + i0^+} \tag{2.22}$$

with $\tilde{\mathcal{D}}_\sigma(\omega) = -\frac{1}{\pi}\operatorname{Im}\tilde{\mathcal{G}}_\sigma(\omega)$ the corresponding spectral density (and $\theta(x)$ the unit step function).

Specifically, the retarded LMA $\Sigma_\uparrow(\omega; T)$ $(= -[\Sigma_\downarrow(-\omega; T)]^*$ by p–h symmetry) is given by

$$\Sigma_\uparrow(\omega; T) = U^2 \int_{-\infty}^\infty \frac{d\omega_1}{\pi} \int_{-\infty}^\infty d\omega_2\, \chi^{+-}(\omega_1; T) \frac{\tilde{\mathcal{D}}_\downarrow(\omega_2)}{\omega + \omega_1 - \omega_2 + i0^+} h(\omega_1; \omega_2) \tag{2.23a}$$

with

$$h(\omega_1; \omega_2) = \theta(\omega_1)f(\omega_2; T) + \theta(-\omega_1)[1 - f(\omega_2; T)] \tag{2.23b}$$

(which reflects the hard-core boson character of the local f-level spin flips [32], whose statistics are dictated by the probability with which fermions can hop from/to site i to/from the surrounding host lattice, as embodied in the Fermi functions). $\chi^{+-}(\omega; T) \geqslant 0$ denotes the (local) spectral density of transverse spin excitations, given by $\chi^{+-}(\omega; T) = \operatorname{sgn}(\omega)\operatorname{Im}\Pi^{+-}(\omega; T)$ with $\Pi^{+-}(\omega; T)$ the retarded, finite-T polarization propagator. The latter is given at the simplest level, considered here, by an RPA-like p–h ladder sum in the transverse spin channel, obtained by straightforward analytical continuation of the imaginary time

$$\Pi^{+-}(i\omega_m) = {}^0\Pi^{+-}(i\omega_m)[1 - U\,{}^0\Pi^{+-}(i\omega_m)]^{-1}. \tag{2.24}$$

The bare polarization bubble diagram ${}^0\Pi^{+-}$ may itself be expressed either in terms of the broken symmetry MF propagators $\{g_\sigma^f(\omega; x)\}$ (section 2.1), as shown explicitly in figure 1(c) of [36] and with the resultant LMA referred to therein as LMA I, or in terms of the self-consistent medium propagators $\{\tilde{\mathcal{G}}_\sigma\}$, correspondingly referred to as LMA II. In practice, as shown in [36], results for single-particle dynamics arising from LMA I/II are very similar, and for that reason explicit results are given in the present paper for LMA I alone. We also add that for $T = 0$, equations (2.23) reduce generally (via equation (2.22)) to

$$\Sigma_\uparrow(\omega; 0) = U^2 \int_{-\infty}^\infty \frac{d\omega_1}{\pi} \chi^{+-}(\omega_1; 0)[\theta(\omega_1)\tilde{\mathcal{G}}_\downarrow^-(\omega_1 + \omega) + \theta(-\omega_1)\tilde{\mathcal{G}}_\downarrow^+(\omega_1 + \omega)] \tag{2.25}$$

as employed (in time-ordered form) for $T = 0$ in [36].

The above considerations specify the LMA two-self-energies that we consider in practice; $\tilde{\Sigma}_\sigma(\omega; T)$ being given in its entirety by equation (2.13), $|\bar{\mu}|$ therein by equation (2.17) and the dynamical $\Sigma_\uparrow(\omega; T)$ by equations (2.23) (with $\Sigma_\downarrow(\omega; T)$ by p–h symmetry). The problem is readily solved numerically. As explained in section 2.1 (following equation (2.16)), for given $\{\tilde{\Sigma}_\sigma\}$ equations (2.9) and (2.16) may be solved straightforwardly for the Feenberg self-energy $S(\omega)$ and the full c/f-electron propagators $G^\nu(\omega)$. An iterative, self-consistent solution is naturally required, since the $\{\tilde{\Sigma}_\sigma\}$ are functionals of the renormalized medium f propagators $\{\tilde{\mathcal{G}}_\sigma\}$, themselves given explicitly by equation (2.21) and thus dependent on $S(\omega)$. Since both $\tilde{\mathcal{G}}_\sigma$ and the MF propagators g_σ^f depend explicitly on $x = \frac{1}{2}U|\mu|$, it is numerically optimal to solve for fixed x, with U determined, as opposed to vice versa [36].

The problem is first solved for $T = 0$, ensuring that SR (equation (2.19)) is satisfied at each iterative step. For any given $x = \frac{1}{2}U|\mu|$ solution of equation (2.19) determines U, and the local moment $|\mu| \equiv |\mu(T = 0)|$ then follows directly. As explained in [36] this step generates a spin-flip resonance in $\chi^{+-}(\omega; T = 0)$ centred on a non-zero frequency ω_m. This is the low-energy scale characteristic of the Kondo lattice (and with $\omega_m \propto Z$, the quasiparticle weight); its origins within the LMA thus stemming from SR, and its physical significance being that it sets the timescale $\tau \sim h/\omega_m$ for restoration of the locally broken symmetry inherent at the crude level of pure MF. For $T > 0$ the same iterative algorithm may be employed, except that SR is no longer required. Temperature enters the problem in two distinct ways: (a) explicitly, and centrally, via the Fermi functions inherent in $h(\omega_1; \omega_2)$ and $\chi^{+-}(\omega_1; T)$ (equation (2.23)), and (b) implicitly, via the T-dependence of the local moment $|\mu| \equiv |\mu(T)|$ in $x = \frac{1}{2}U|\mu|$. The latter may be encompassed via $|\mu(T)| = |\mu(0)| + \delta|\mu(T)|$, with $|\mu(0)|$ the $T = 0$ moment required to satisfy SR as above, and with $\delta|\mu(T)|$ calculated in practice at MF level [32], such that $\delta|\mu(0)| = 0$. As for the AIM [32], we find however that the resultant T-dependence of $|\mu|$ is negligible for essentially all (U, V) (provided one is not concerned with physically irrelevant temperatures of the order of U), and we thus omit it from the results shown explicitly in section 4.

3. Electrical transport and optical conductivity

Within the large-dimensional framework of DMFT a knowledge of single-particle dynamics, in particular the (ω, T)-dependences of the f-electron self-energy $\Sigma_f(\omega; T)$, enable $q = 0$ transport properties to be determined [8–11]. In this section we specify some basic results for the conduction electron scattering rate and ω-dependent electrical conductivity, for both the hypercubic and BLs. These are independent of the particular approximation employed to determine $\Sigma_f(\omega; T)$. But they naturally underlie the results obtained via the LMA that are given in section 5.

Equation (2.7) for the conduction electron Green function, $G^c(\omega) = \mathrm{H}(\gamma)$ with $\gamma(\omega) = \omega^+ - V^2[\omega^+ - \Sigma_f(\omega; T)]^{-1}$, is equivalently but more familiarly expressed as $G^c(\omega) = N^{-1} \sum_\alpha [\omega^+ - \epsilon_\alpha - \Sigma_c(\omega; T)]^{-1}$. Here ϵ_α denote the states of the free ($V = 0$) conduction band with density of states (equation (2.4)) $\rho_0(\epsilon) = N^{-1} \sum_\alpha \delta(\epsilon - \epsilon_\alpha)$ (e.g. $\epsilon_\alpha \equiv \epsilon_k$ for a Bloch decomposable lattice); and $\Sigma_c(\omega; T)$ ($= \omega^+ - \gamma(\omega)$) is the purely local conduction electron self-energy, related to the f-electron single self-energy Σ_f by

$$\Sigma_c(\omega; T) = V^2[\omega^+ - \Sigma_f(\omega; T)]^{-1}. \tag{3.1}$$

It will prove useful in the following to rewrite equation (2.7) as

$$G^c(\omega) = \int_{-\infty}^{\infty} d\epsilon \, \rho_0(\epsilon) G^c(\epsilon; \omega) \equiv \langle G^c(\epsilon; \omega) \rangle_\epsilon \tag{3.2}$$

with the ϵ-resolved propagator $G^c(\epsilon; \omega) = [\gamma(\omega) - \epsilon]^{-1} = [\omega^+ - \epsilon - \Sigma_c(\omega; T)]^{-1}$ and corresponding spectrum $D_c(\epsilon; \omega) = -\frac{1}{\pi} \mathrm{Im}\, G^c(\epsilon; \omega)$; and where $\langle A(\epsilon)\rangle_\epsilon = \int \mathrm{d}\epsilon\, \rho_0(\epsilon)\, A(\epsilon)$ defines the ϵ-average of any $A(\epsilon)$.

In particular, the conduction electron scattering rate $1/\tau(\omega; T)$ ($\hbar = 1$) considered in section 4.1, is given by

$$\frac{1}{\tau(\omega; T)} = \gamma_I(\omega; T) = - \mathrm{Im}\, \Sigma_c(\omega; T) \tag{3.3}$$

(with $\gamma_I = \mathrm{Im}\, \gamma$). It is conveniently expressed in the dimensionless form $1/\tilde{\tau}(\omega; T) = \tilde{\gamma}_I(\omega; T) = \pi \rho_0 \gamma_I(\omega; T)$, with $\rho_0 = \rho_0(\epsilon = 0)$; and is given in terms of the f-electron self-energy $\Sigma_f = \Sigma_f^R - i\Sigma_f^I$ by

$$\frac{1}{\tilde{\tau}(\omega; T)} = \tilde{\gamma}_I(\omega; T) = \frac{\Delta_0^{-1}\Sigma_f^I(\omega; T)}{[\omega' - \Delta_0^{-1}\Sigma_f^R(\omega; T)]^2 + [\Delta_0^{-1}\Sigma_f^I(\omega; T)]^2} \tag{3.4}$$

where $\omega' = \omega/\Delta_0$ and Δ_0 is defined by

$$\Delta_0 = \pi V^2 \rho_0. \tag{3.5}$$

Physically, Δ_0 is the hybridization strength that would arise for a pure AIM, in which a single correlated f level is locally coupled (via V) to the free metallic conduction band $\rho_0(\epsilon)$. Equation (3.4) will prove important in connecting results for the PAM at large ω and/or T to those for the pure AIM itself (and notwithstanding the fact that the ground state for the latter is metallic, while that for the symmetric PAM is of course insulating); see also equation (3.12) below.

Calculation of the ω-dependent conductivity is in principle straightforward in the large-dimensional limit of DMFT, since the strict absence of vertex corrections [41] to the ($q = 0$) current–current correlation function means that only the lowest-order conductivity bubble diagram survives [8–11]. We denote the trace of the resultant conductivity tensor by $\tilde{\sigma}(\omega; T)$ ($\frac{1}{3}$ of which, denoted by $\sigma(\omega; T)$, provides an approximation to the isotropic conductivity for a $d = 3$-dimensional system). This may be cast in the form

$$\frac{\tilde{\sigma}(\omega; T)}{\sigma_0} = F_\alpha(\omega; T) \tag{3.6}$$

where $\sigma_0 = \frac{\pi e^2 a^2}{\hbar} \frac{N}{V} \simeq \frac{\pi e^2}{\hbar a}$ such that $\sigma_0 \sim 10^4$–10^5 Ω^{-1} cm^{-1} for lattice constants a in the physically realistic regime of 1–10 Å. The dimensionless $F_\alpha(\omega; T)$ depends on the lattice type, and is given explicitly for the HCL and BL by

$$F_{HCL}(\omega; T) = \frac{t_*^2}{\omega} \int_{-\infty}^{\infty} \mathrm{d}\omega_1 \, [f(\omega_1) - f(\omega_1 + \omega)]\langle D_c(\epsilon; \omega_1) D_c(\epsilon; \omega_1 + \omega)\rangle_\epsilon \tag{3.7a}$$

$$F_{BL}(\omega; T) = \frac{t_*^2}{\omega} \int_{-\infty}^{\infty} \mathrm{d}\omega_1 \, [f(\omega_1) - f(\omega_1 + \omega)]\langle D_c(\epsilon; \omega_1)\rangle_\epsilon \langle D_c(\epsilon; \omega_1 + \omega)\rangle_\epsilon \tag{3.7b}$$

(with $f(\omega)$ here the Fermi function). The exact result equation (3.7a) for the HCL is of course well known (see e.g. [8–11]) and widely used even in studies employing the BL (e.g. [21]); although for the latter we emphasize that it is equation (3.7b) which follows from direct analysis of the conductivity bubble diagram. Equations (3.7a) and (3.7b) correspond in an obvious physical sense to limiting forms of behaviour, from fully correlated to uncorrelated averages of the $D_c(\epsilon; \omega)$. Both will be considered in section 5ff.

Before proceeding, we comment briefly on evaluation of $F_{HCL}(\omega; T)$ itself, under a single approximation: namely that in $\langle D_c(\epsilon; \omega_1) D_c(\epsilon; \omega_1 + \omega) \rangle_\epsilon = \int_{-\infty}^{\infty} d\epsilon \, \rho_0(\epsilon) \, D_c(\epsilon; \omega_1) D_c(\epsilon; \omega_1 + \omega)$ entering equation (3.7a) the ϵ dependence of $\rho_0(\epsilon)$ is neglected, $\rho_0(\epsilon) \simeq \rho_0(0) \equiv \rho_0$. A straightforward integration over $\epsilon \in (-\infty, \infty)$ then yields

$$\langle D_c(\epsilon; \omega_1) D_c(\epsilon; \omega_1 + \omega) \rangle_\epsilon \simeq \frac{\rho_0}{\pi} \frac{[\gamma_I(\omega_1 + \omega) + \gamma_I(\omega_1)]}{[\gamma_R(\omega_1 + \omega) - \gamma_R(\omega_1)]^2 + [\gamma_I(\omega_1 + \omega) + \gamma_I(\omega_1)]^2} \tag{3.8}$$

(where $\gamma(\omega) = \gamma_R(\omega) + i\gamma_I(\omega)$). Use of this in equation (3.7a), relating γ to the conduction electron self-energy Σ_c as above, gives

$$F_{HCL}(\omega; T) \simeq \frac{-\rho_0 t_*^2}{\pi \omega} \text{Im} \int_{-\infty}^{\infty} d\omega_1 \frac{[f(\omega_1) - f(\omega_1 + \omega)]}{\omega - \Sigma_{c,r}(\omega_1 + \omega) + \Sigma_{c,a}(\omega_1)} \tag{3.9}$$

where r/a here denote retarded/advanced functions; and for the particular case of the dc limit $\omega = 0$, equation (3.8) with equations (3.4) and (3.7a) gives

$$F_{HCL}(0; T) \simeq \frac{1}{2} [\rho_0 t_*]^2 \int_{-\infty}^{\infty} d\omega \frac{-\partial f(\omega)}{\partial \omega} \tilde{\tau}(\omega; T) \equiv \frac{1}{2} [\rho_0 t_*]^2 \langle \tilde{\tau} \rangle. \tag{3.10}$$

Equations (3.9) and (3.10) are likewise well known [25] and widely used; and the latter in particular, expressing the dc conductivity in terms of an averaged scattering time, is physically intuitive. We emphasize nevertheless that they are approximate (granted even the legitimate neglect of vertex corrections), being dependent on the 'flat-band' approximation $\rho_0(\epsilon) \simeq \rho_0 \forall \epsilon$ as above; and it is in fact simple to show that this approximation by itself fails to account for the existence of the Kondo insulating gap that is characteristic of the symmetric PAM. That said, however, one expects physically that equation (3.10) should provide a good approximation to the dc conductivity at least for sufficiently high temperatures dominated by incoherent scattering: the question here, considered briefly in section 5, being 'how high is high?'.

Finally, for explicit use in section 5, we consider the pure AIM itself, denoting by $\rho_{imp}(T)$ the change in resistivity due to addition of the impurity to the non-interacting host, and $\rho'_{imp}(T) = \rho_{imp}(T)/\rho_{imp}(0)$. This has the same functional form as equation (3.10), namely (see e.g. [2])

$$\frac{1}{\rho'_{imp}(T)} = \int_{-\infty}^{\infty} d\omega \frac{-\partial f(\omega)}{\partial \omega} \tilde{\tau}_{imp}(\omega; T). \tag{3.11}$$

The impurity scattering rate is given by [2] $1/\tilde{\tau}_{imp}(\omega; T) = \pi \Delta_0 D_{imp}(\omega; T)$ with $D_{imp}(\omega; T)$ the impurity spectral function and Δ_0 the hybridization strength equation (3.5) (such that $\pi \Delta_0 D_{imp}(0; 0) = 1$ from the Friedel sum rule [2]). Denoting the impurity single self-energy by $\Sigma(\omega; T) = \Sigma^R(\omega; T) - i\Sigma_I(\omega; T)$, the impurity transport rate is given explicitly by

$$\frac{1}{\tilde{\tau}_{imp}(\omega; T)} = \frac{[1 + \Delta_0^{-1} \Sigma^I(\omega; T)]}{[\omega' - \Delta_0^{-1} \Sigma^R(\omega; T)]^2 + [1 + \Delta_0^{-1} \Sigma^I(\omega; T)]^2} \tag{3.12}$$

with $\omega' = \omega/\Delta_0$, which should be compared to its counterpart for the PAM, equation (3.4).

4. Single-particle dynamics

We turn now to single-particle spectra resulting from the LMA specified in section 2. Our focus for obvious physical reasons is the strong-coupling (large-U) Kondo lattice regime, wherein universality arises: in particular the resultant scaling behaviour of dynamics, and the thermal destruction of the Kondo (insulating) gap. Conduction electron scattering rates $1/\tilde{\tau}(\omega; T)$ are also considered here (section 4.1) since these are closely related to single-particle dynamics (as directly evident from equation (3.4)).

In strong coupling, as shown in [36] for $T = 0$ and consistent with previous work [12–15, 24, 28, 29], the problem is characterized by a single low-energy scale, as embodied in Δ_g given by

$$\Delta_g = Z \frac{V^2}{t_*} \tag{4.1}$$

with $Z = [1 - (\partial \Sigma_f^R(\omega; 0)/\partial \omega)_{\omega=0}]^{-1}$ the quasiparticle weight. This sets the scale for the Kondo gap, which (section 2.1) is generically hard (as for the BL), albeit strictly soft for the HCL; other embodiments of this low-energy scale, such as the spin flip ω_m arising in $\chi^{+-}(\omega; 0)$ (section 2.2 and [36]) are equivalent to Δ_g, being simply proportional to it. There are two distinct issues relating to the low-energy scale. The first is its dependence on the 'bare' high-energy parameters entering the Hamiltonian, namely the f-electron Coulomb repulsion U, hybridization V and bandwidth scale t_* (or equivalently $\rho_0^{-1} \propto t_*$). In strong coupling it is known, from NRG results in particular [13], that the gap scale becomes exponentially small; such behaviour is indeed found within the LMA (namely $\ln \Delta_g \propto -U/(8V^2\rho_0)$ as detailed in [36]). This is important insofar as it guarantees a clean separation between low-energy and/or temperature scales on the order of the Kondo gap and multiples of it, and high-ω and/or T on the order of the bare energy scales (Hubbard satellites in the f-electron spectra to cite an extreme). Failure to recover this pristine separation of scales can obscure much relevant physics in the strong-coupling regime (we provide examples in the following sections). This may arise either because strong coupling and/or low temperatures are difficult to access in a numerical approach (e.g. QMC), or because the approximate theory used leads to an insufficiently small low-energy scale, for example algebraic rather than exponential decay in U. IPT [10, 21, 22] provides an example of the latter, and is discussed further in the following sections.

Granted a clean separation of energy scales however, the precise dependence of the gap scale Δ_g on bare parameters is subsidiary. Of primary importance is that physical properties, whether dynamics or transport, exhibit universal scaling behaviour on experimentally relevant 'low'-ω and/or T scales on the order of the Kondo gap and (in principle arbitrary) multiples thereof. The scaling is of course in terms of the gap Δ_g itself, and is thus *independent* of the bare model parameters, in contrast to the correspondingly non-universal behaviour arising on truly high-ω or T scales characteristic of the bare parameters. Neither is such scaling of purely theoretical interest, for an experimental gap of (say) 50 K $\sim$ 4 meV is tiny on the electron volt scale typical of bare parameters, and many multiples of it may arise before non-universal scales are reached in practice. Moreover, it is arguably less preferable, as well as unnecessary in general, to have comparison to the ω and/or T dependence of experiment hinge on a particular choice of bare model parameters, as opposed to a knowledge solely of the experimental gap scale, which alone is required if comparison is made instead to the relevant scaling form (section 7).

Figure 2 summarizes salient results for the $T = 0$ f-electron spectrum [36], showing $\pi \Delta_0 D^f(\omega)$ (with $\Delta_0 = \pi V^2 \rho_0$, equation (3.5)) as a function of $\tilde{\omega} = \omega/\Delta_g$, and for both the BL (solid curve) and HCL (dashed). This is the universal scaling form arising from the LMA[5], with no dependence whatever on any of the bare parameters U, V, t_*. It naturally depends on the lattice type, but only weakly and on scales up to a few times the gap, beyond which the two scaling spectra coincide. The Kondo insulating gap is directly apparent in figure 2. For the BL we also show explicitly the limiting quasiparticle form, whose recovery at sufficiently low $\tilde{\omega}$ embodies adiabatic continuity to the non-interacting limit ('insulating Fermi liquid' behaviour, section 2.1 and [36]), given explicitly using equation (2.20b) by

---

[5] The small spectral 'dip' at $|\omega|/\Delta_g \sim 5$ is known [30–36] to be entirely an artifact of the specific RPA-like form employed for Π^{+-}; it can be removed [31], but we are content to live with it here.
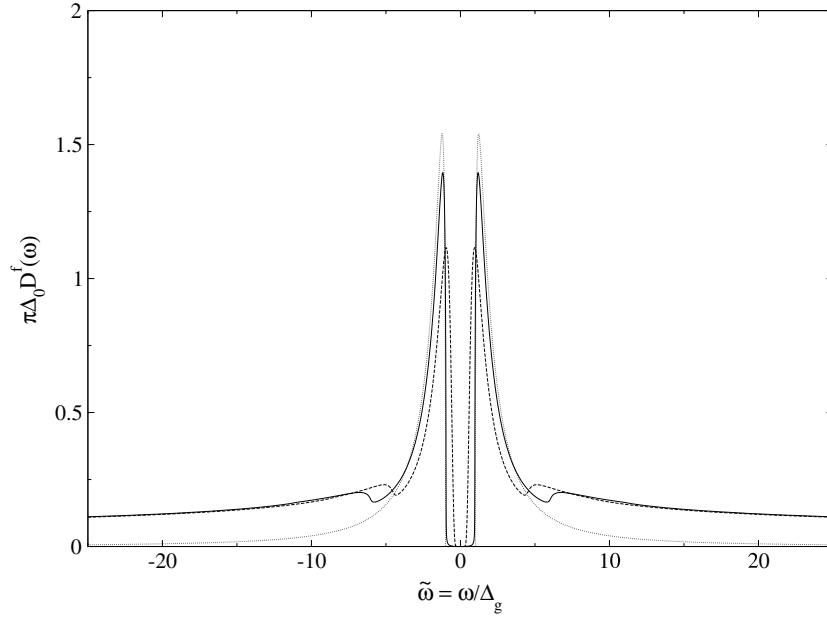
Figure 2. $T = 0$ scaling spectra $\pi \Delta_0 D^f(\omega)$ versus $\tilde{\omega} = \omega/\Delta_g$ for the BL (solid curve) and the HCL (dashed curve). The limiting low-energy quasiparticle form is also shown (for the BL, dotted curve).

$\pi \Delta_0 D^f(\omega) \sim (4/|\tilde{\omega}|^2)[1 - 1/\tilde{\omega}^2]^{\frac{1}{2}}$ for $|\tilde{\omega}| > 1$ (and zero for $|\tilde{\omega}| = |\omega|/\Delta_g < 1$, the gap). For $|\tilde{\omega}| \gtrsim 3$ however the quasiparticle form is simply inadequate: it decays rapidly as $\sim 1/|\tilde{\omega}|^2$ and fails to recover the long, slowly decaying tails evident in figure 2. The latter, which dominate the scaling spectra at (moderate to) large $\tilde{\omega}$—and in consequence transport properties at correspondingly 'high' temperatures (section 5)—are logarithmically slow and discussed further in the following sections. Universal scaling in terms of $\tilde{\omega}$ is not of course confined to the f-electron spectra: the $T = 0$ c-electron spectrum $t_* D^c(\omega)$ (or equivalently $D^c(\omega)/\rho_0$) behaves likewise; and in consequence, as follows straightforwardly using equations (2.5), $\Delta_0^{-1} \Sigma_f(\omega; 0)$ also scales universally (which is why the dimensionless conduction electron scattering rate has been defined as in equation (3.4)).

For finite temperatures, what one expects in scaling terms is obvious: namely that the f/c spectra and f-electron self-energy should now exhibit universal scaling in terms of both $\tilde{\omega} = \omega/\Delta_g$ *and* $\tilde{T} = T/\Delta_g$. That such scaling correctly arises within the LMA is demonstrated in figure 3 where, for fixed $\tilde{T} = 2$, the f- and c-electron scaling spectra are shown for three different interaction strengths $\tilde{U} = U/t_* = 5.6, 6.1$ and 7.0 and $V^2/t_*^2 = 0.2$. The inset shows $\pi \Delta_0 D^f(\omega)$ on an 'absolute' scale, i.e. versus ω/t_*, illustrating the exponential reduction in the gap scale with increasing interaction strength. The main figures by contrast show the f/c spectra versus $\tilde{\omega} = \omega/\Delta_g$, from which the scaling collapse is evident (and in practice sets in by rather moderate interactions $\tilde{U} \sim 4$ or so).

The scaling illustrated above arises generically, and figure 4 shows the resultant LMA scaling spectra (for the BL) for a range of scaled temperatures up to $\tilde{T} = 25$. The thermal destruction/infill of the Kondo insulating gap is evident, occurring as expected physically for temperatures on the order of the gap Δ_g, and accompanied in the case of the f-electron spectra by a corresponding destruction of the characteristic $T = 0$ spectral 'horns'. We also note, as
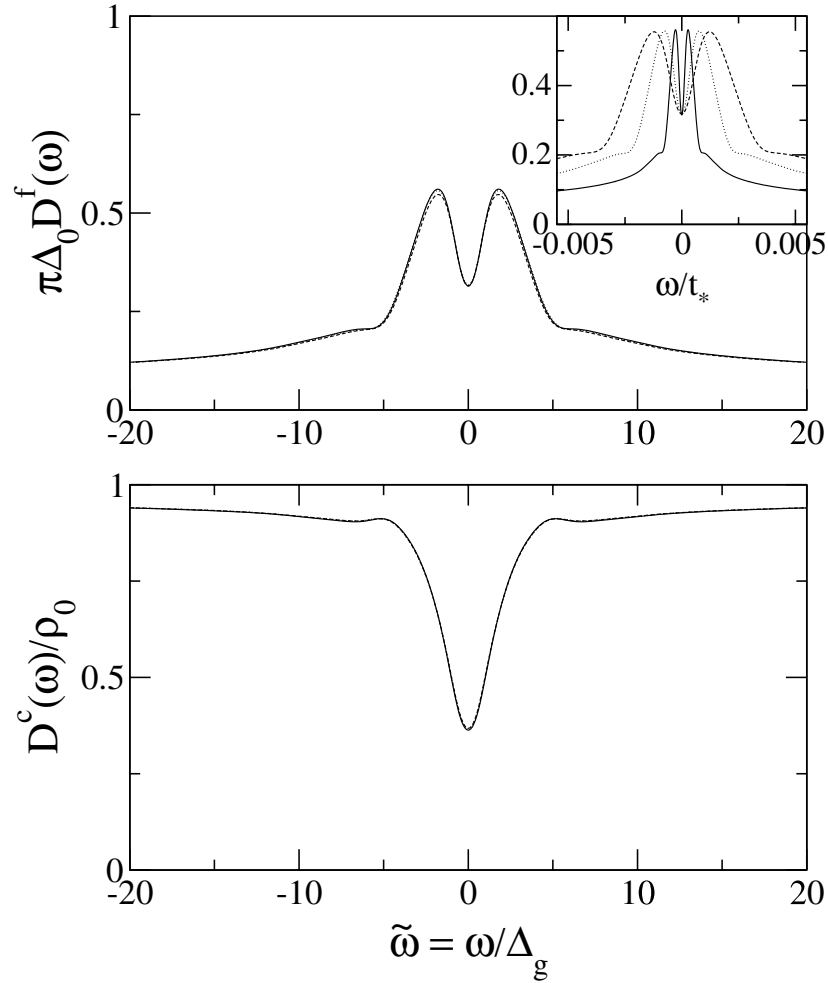
Figure 3. Universal scaling spectra (BL) for fixed $\tilde{T} = T/\Delta_g = 2 : \pi\Delta_0 D^f(\omega)$ and $D^c(\omega)/\rho_0$ versus ω/Δ_g for $V^2/t_*^2 = 0.2$ and $\tilde{U} = U/t_* = 5.6$ (dashed), 6.1 (dotted) and 7.0 (solid). Inset: corresponding f spectra on an absolute scale, versus ω/t_*.

evident from the inset to the f spectrum which shows the spectrum on an enlarged $\tilde{\omega}$ scale, that for any $\tilde{T}$ the high-frequency asymptotics of the scaling spectra coincide with that for $\tilde{T} = 0$; as likewise expected physically, and which behaviour arises for frequencies $|\tilde{\omega}| \gg \tilde{T}$.

To give an 'all scales' perspective on thermal evolution, figure 5 shows the f- and c-electron spectra for the BL (specifically for $\tilde{U} = 6.1$ and $V^2/t_*^2 = 0.2$) on an absolute energy scale, versus ω/t_*, and for temperatures $\tilde{T} = T/\Delta_g = 0, 10, 50$ and 450. The f spectrum is naturally dominated by the non-universal Hubbard satellites at $|\omega| \sim \frac{U}{2}$ which carry almost all the spectral weight (and are of course 'projected out' of the scaling spectra), the key low-energy universal spectral features shown in figures 2–4 being nigh on invisible in figure 5 as expected, since their net spectral weight is of order $Z \ll 1$. The c spectrum, which shows weakly remnant Hubbard peaks, is by contrast dominated by the envelope of the free conduction band (the $|\omega| \leqslant t_*$ semiellipse for the BL); and again the thermal destruction of
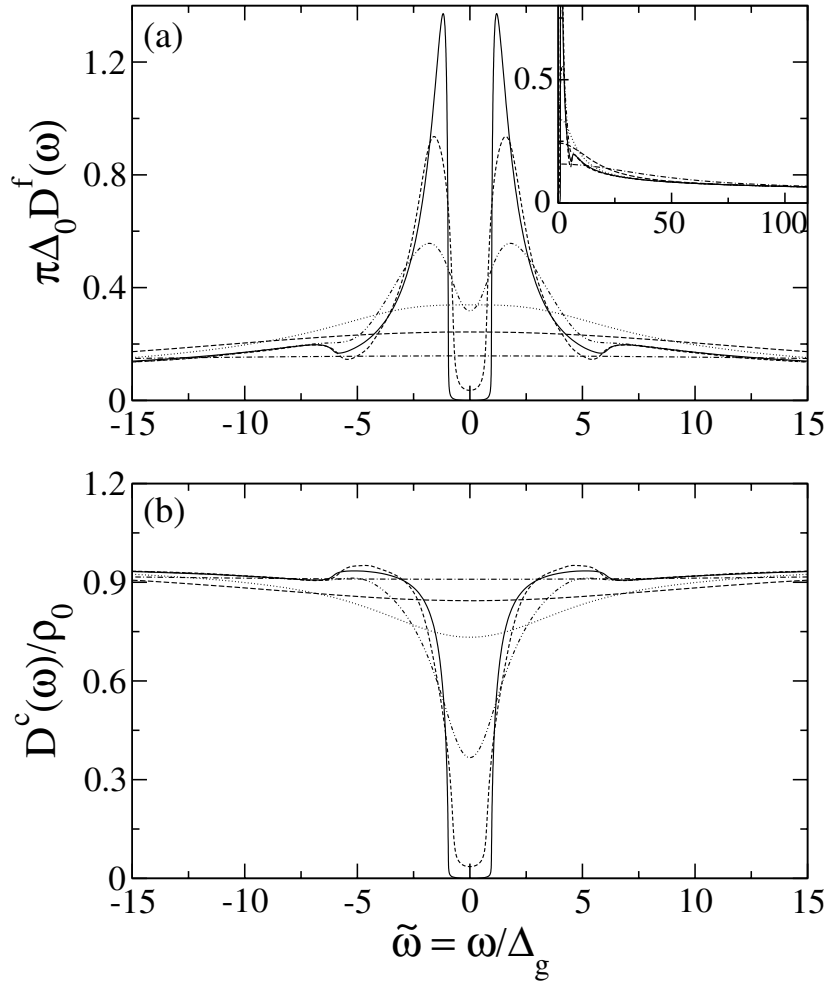
Figure 4. Temperature dependence of the BL scaling spectra: $\pi \Delta_0 D^f(\omega)$ and $D^c(\omega)/\rho_0$ versus ω/Δ_g for temperatures $\tilde{T} = T/\Delta_g = 0$ (solid), 1 (short dash), 2 (double point–dash), 5 (dotted), 10 (long dash) and 25 (point–dash). Inset: f spectra on an enlarged scale, out to $\tilde{\omega} = 100$.

the low-energy spectral gap is barely visible. We add moreover that until temperature reaches essentially non-universal scales, the T-dependence of single-particle dynamics is confined to the relevant low energies illustrated in figures 3 and 4 (see e.g. the inset to figure 5 where the Hubbard satellites are enlarged, noting that $\tilde{T} = 450$ here corresponds to $T \sim 0.2t_*$).

4.1. Scattering rates

The conduction-electron scattering rates $\tau^{-1}(\omega; T)$ are now considered. These are directly related to the f-electron self-energy $\Delta_0^{-1}\Sigma_f(\omega; T)$ as in equations (3.3) and (3.4), and determine the conductivity via the dependence thereof (equation (3.7)) on the c-electron spectrum $D_c(\epsilon; \omega)$ (or rather more directly via equation (3.10) in the latter's regime of applicability, considered explicitly in section 5).

Before proceeding we note that our conclusions regarding the scattering rates differ significantly from the work of [21]. In order to explain typical experimental conductivities
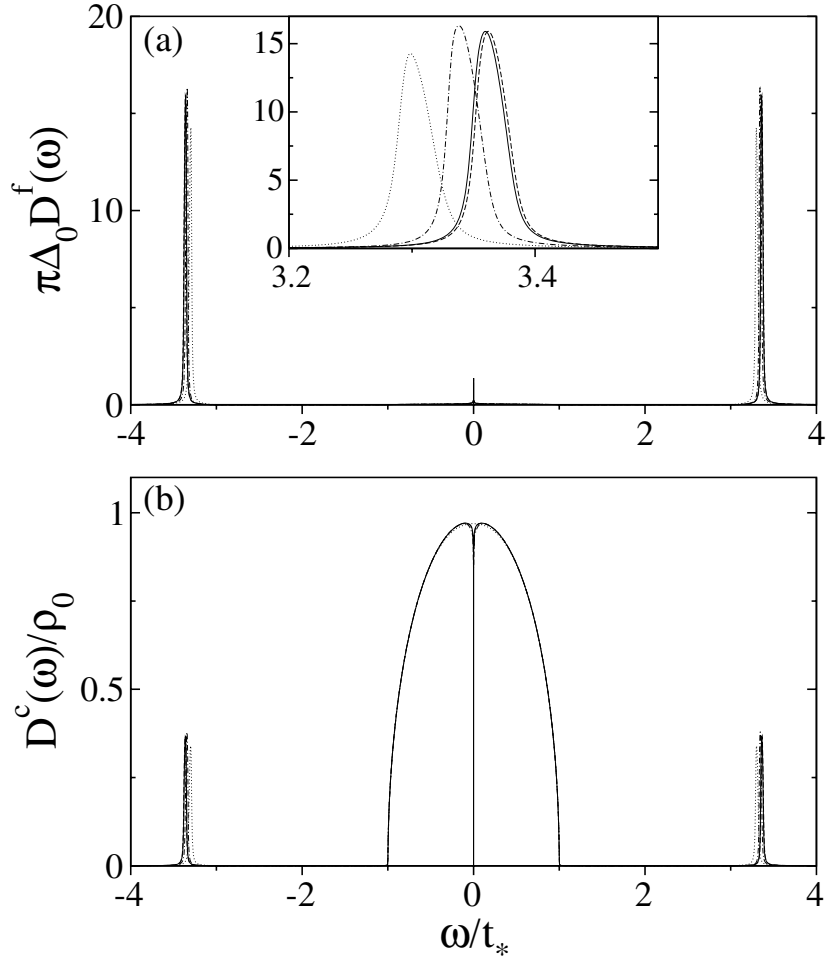
Figure 5. Spectra on all scales (BL with $U/t_* = 6.1$ and $V^2/t_*^2 = 0.2$): $\pi\Delta_0 D^f(\omega)$ and $D^c(\omega)/\rho_0$ versus ω/t_* for temperatures $\tilde{T} = T/\Delta_g = 0$ (solid), 10 (dashed), 50 (point–dash) and 450 (dotted). Inset: Hubbard satellites on a much reduced scale.

for Kondo insulators, it was argued in [21] that scattering rates in the vicinity of the Fermi level should be on the order of $\sim$0.1–1 of the bandwidth t_* (values some two to three orders of magnitude higher than for a clean metal like Cu). Scattering rates calculated in [21] were however found to be some one to two orders of magnitude lower than required. While the authors of [21] note that this behaviour is very surprising, they attribute it to an intrinsic limitation of the model itself, rather than e.g. to a limitation of the approximate calculations employed, or to a possible misidentification of the relevant temperature scales involved. We find by contrast, as shown below, that scattering rates can certainly attain values on the order of the bandwidth t_*; and indeed argue that rates of this order *must* arise over a wide, experimentally relevant temperature regime.

The ω- and T-dependences of the scattering rate arising in strong coupling are illustrated in figure 6: namely $\tau^{-1}(\omega; T)$ in units of the bandwidth t_*, versus $\tilde{\omega} = \omega/\Delta_g$ and for a range of
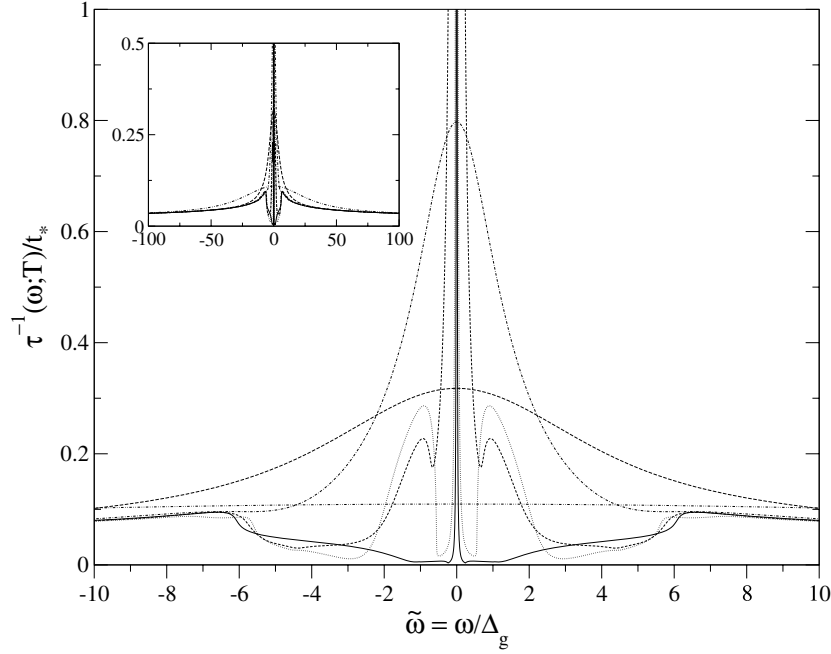
Figure 6. Thermal evolution of the conduction-electron scattering rates: $\tau^{-1}(\omega; T)$ (in units of the BL bandwidth t_*) versus $\tilde{\omega} = \omega/\Delta_g$ for temperatures $\tilde{T} = T/\Delta_g = 0.1$ (solid), 0.5 (dotted), 1 (short dash), 2.5 (point–dash), 5 (long dash) and 20 (double point–dash). Inset: on an expanded scale, out to $\tilde{\omega} = 100$.

temperatures $\tilde{T} = T/\Delta_g$ from 0.1 to 20, as given explicitly via equation (3.4) (where the 'bare' factor of $\omega' \equiv \tilde{\omega}\frac{\Delta_g}{\Delta_0}$ plays no role since $\frac{\Delta_g}{\Delta_0} \propto Z$ is exponentially small in strong coupling). The inset to figure 6 shows the same results on an expanded scale out to $\tilde{\omega} = 100$ (showing that for $|\tilde{\omega}| \gg \tilde{T}$ the 'tail' behaviour reduces to that characteristic of $T = 0$, the logarithmically slow decay of which is considered explicitly below, figure 8). The only remaining ω-dependence arises on non-universal (and essentially irrelevant) scales on the order of the Hubbard satellites $|\omega| \sim \frac{U}{2}$, where as expected physically the scattering rate is strongly peaked [21]; this is omitted from figure 6 for obvious reasons.

The first point to note about $\tau^{-1}(\omega; T)$ is that for $T = 0$ precisely it contains a δ-function contribution at the Fermi level $\omega = 0$; specifically $\pi t_* \delta(\tilde{\omega})$ as follows generally via equation (3.4) using $\Sigma_f^R(\omega; 0) \sim -\frac{\omega}{Z}$ as $\omega \to 0$. For $T \neq 0$ this becomes the resonance evident in figure 6, which naturally broadens with increasing temperature; and the *only* thermal scale on which this can occur is the gap Δ_g—the single low-energy scale characteristic of the system in strong coupling. This argument is rather general. The scattering rate in the vicinity of the Fermi level, $|\tilde{\omega}| \lesssim \tilde{T}$, in consequence diminishes with increasing $\tilde{T}$ from essentially arbitrarily large values (reflecting the insulating nature of the $T = 0$ state); and does so on temperature scales of the order of the gap, Δ_g. The results of figure 6 show moreover that for temperatures $\tilde{T} = T/\Delta_g$ in the range $\sim$1–20, scattering rates in the relevant $\tilde{\omega}$ regime are *indeed on the order of* $\sim$0.1–1 *of the bandwidth* t_*. We also add that while a temperature range of this order certainly encompasses that relevant to experiment (section 7), the essential point is not dependent on it, since for $\tilde{T} \gg 1$ we find the Fermi level scattering rate to decay slowly with temperature (specifically $\tau^{-1}(\omega = 0; T) \propto 1/\ln^2(\tilde{T})$, see equation (5.7) below).

The issue of scattering rates was considered in [21] using IPT[6], explicitly so for a particular choice of bare parameters $U/t_* = 3$ and $V/t_* = 0.25$, and at a temperature $T = 0.1t_*$, a significant fraction of the free conduction bandwidth and some 50 times the corresponding IPT gap $\Delta_g \equiv ZV^2/t_*$. The resultant scattering rate in the vicinity of the Fermi level was found to be $\tau^{-1}(0; T) \sim 10^{-2}t_*$, with which the authors of [21] support their view mentioned above. We have also performed IPT calculations for the same U and V; and indeed for $T = 0.1t_*$ recover the results of [21]. We have further investigated the T-dependence of IPT over a wide $\tilde{T} = T/\Delta_g$ range (as well as a broad (U, V) range). Significantly, we find that for temperatures $\tilde{T}$ up to ~ 5, the behaviour of the resultant $\tau^{-1}(\omega; T)$ is qualitatively similar to that shown in figure 6: in particular, scattering rates in the vicinity of the Fermi level are again found to lie in the range $0.1t_*$–t_*. For temperatures $\tilde{T} \gtrsim 3$–5, the IPT scattering rates decay much more rapidly with increasing $\tilde{T}$ than those arising from the LMA. This reflects the inability of IPT to capture the logarithmically slow decays in $\tilde{\omega}$ and/or $\tilde{T}$ that are characteristic of the model in the strong-coupling/scaling regime, as illustrated below (figure 9); and is in turn related to the fact that IPT leads to an algebraically rather than an exponentially small gap scale in strong coupling, and hence does not produce a 'clean' separation of low/high energy scales. Nonetheless, if it were indeed the case that non-universal temperature scales on the order of e.g. $0.1t_*$ were pertinent in relation to experiment, then the resultant scattering rates would in general be too small to explain observed conductivities. Our view is that this is *not* the case, but rather that the relevant thermal scale for comparison to experiment is the gap Δ_g and multiples of it; on which scales the transport rates readily attain values on the order of $\sim 0.1t_*$–t_*. Further support for this view will be provided in the following sections.

We turn now to more detailed consideration of the conduction-electron scattering rate in strong coupling, in particular its high-frequency 'tail' behaviour evident in figure 6 (inset) and its relation to the f-electron single-particle spectrum. We begin with the latter. It is straightforward to show generally (using equations (2.5) together with the definition equation (2.8) of $\gamma(\omega)$ and equation (3.4)) that the asymptotic behaviour of the dimensionless scattering rate $\tilde{\tau}^{-1}(\omega; T)$ (equation (3.4)) in fact coincides with the f spectrum, namely

$$\frac{1}{\tilde{\tau}(\omega; T)} \sim \pi \Delta_0 D^f(\omega). \tag{4.2}$$

This holds asymptotically for $\tilde{\tau}^{-1}(\omega; T) \ll 1$, which in practice means $(|\omega|/\Delta_g =)|\tilde{\omega}| \gg 1$ for any $\tilde{T}$ (the 'tails') or $\tilde{T} \gg \max(1, |\tilde{\omega}|)$ for any $\tilde{\omega}$. This is illustrated in figure 7(a) for $\tilde{T} = 0$, where the $\tilde{\omega}$-dependences of $\pi\Delta_0 D^f(\omega)$ and $\tilde{\tau}^{-1}(\omega; T)$ are compared (omitting the $\delta(\tilde{\omega})$ contribution for clarity): they naturally differ very significantly at low frequencies, but for $|\tilde{\omega}| \gtrsim 10$ or so their tails rapidly become coincident. The same holds at finite $\tilde{T}$ as illustrated in figure 7(b) for $\tilde{T} = 2.5$ and 10; and for $\tilde{T} \gg 1$ the two coincide asymptotically for all $\tilde{\omega}$.

An obvious question arises: what is the functional form of the $|\tilde{\omega}| \gg 1$ 'tails' in $\tilde{\tau}^{-1}(\omega; T)$ (or equivalently $\pi\Delta_0 D^f(\omega)$), which as seen in figure 6 (inset) arise at sufficiently high frequencies for any temperature $\tilde{T}$? For large $|\tilde{\omega}|$ and/or $\tilde{T}$ one expects [1, 2] on physical grounds that properties of the Kondo lattice such as the f-electron spectrum or the resistivity $\rho(T)$ (section 5) should asymptotically approach those of an AIM (i.e. the pure Kondo model in strong coupling). The high-frequency behaviour of the impurity single-particle scaling spectrum $D_{imp}(\omega)$ for the AIM has only recently been uncovered, using the LMA [31] (which gives excellent agreement with NRG results [34] for that problem). On the testable assumption

---

[6] Exact diagonalization (ED) was also considered in [21]. But *eight*-site ED [21] produces only four significant poles in the 'full' ω-range $0 < \omega \lesssim \frac{U}{2}$, and cannot resolve the relevant low-energy scales. Further, to calculate $\tau^{-1}(\omega; T)$ its poles must be rendered continuous by the addition of an *ad hoc* broadening factor, typically [21] on the order of $0.1t_*$—which is non-universal and enormous relative to the gap.
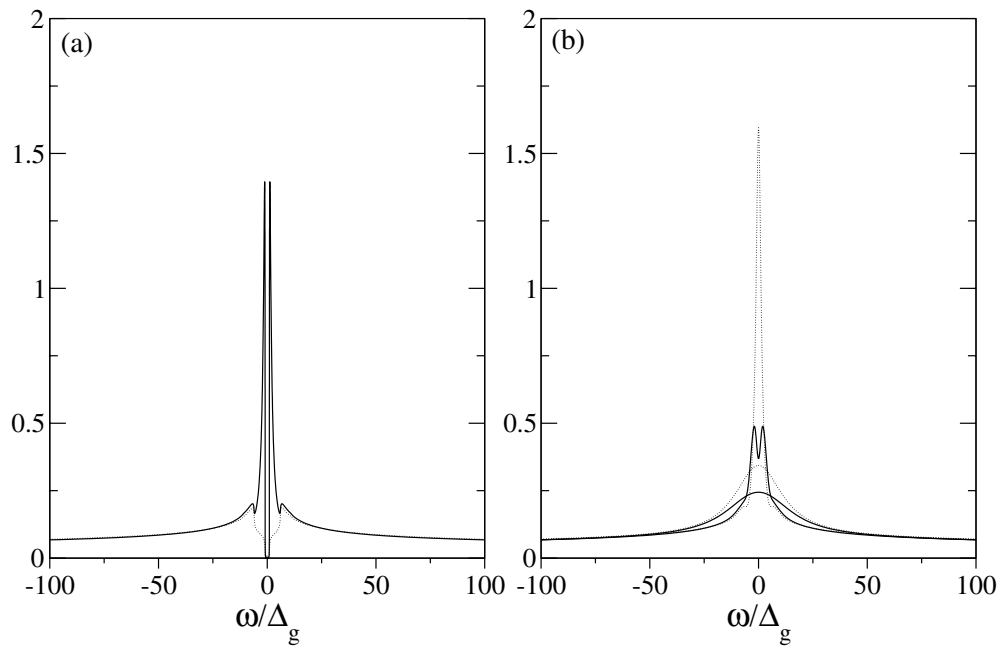
Figure 7. $\pi\Delta_0 D^f(\omega)$ (solid curves) and scattering rates $\tilde{\tau}^{-1}(\omega; T)$ (dotted curves) versus ω/Δ_g (for the BL). (a) $\tilde{T} = T/\Delta_g = 0$; (b) $\tilde{T} = 2.5$ and 10 (in an obvious sequence).
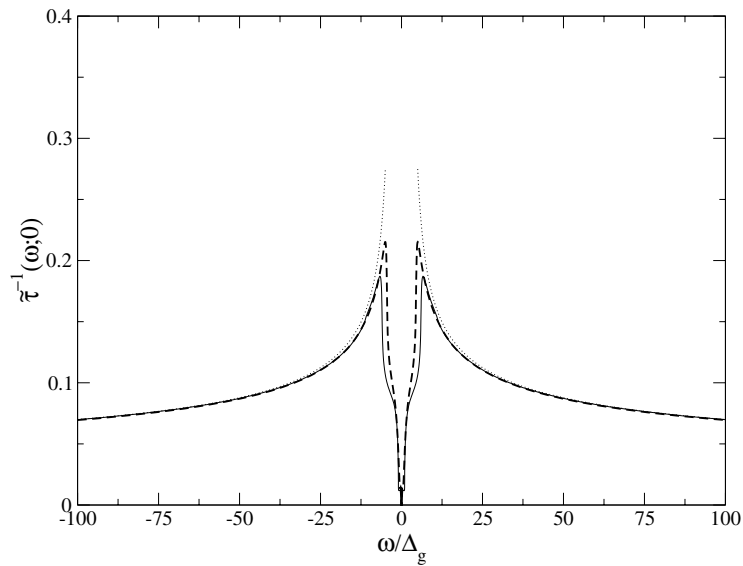

Figure 8. $T = 0$ scattering rates $\tilde{\tau}^{-1}(\omega; 0)$ versus ω/Δ_g for the BL (solid curve) and HCL (dashed curve). Explicit comparison is also made to the asymptotic behaviour equation (4.4) (dotted curve).

that the high-frequency behaviour of the f-electron self-energy for the PAM has the same scaling form as that for the AIM, we thus expect $\Delta_0^{-1}\Sigma_f(\omega)$ to behave as [31]

$$\Delta_0^{-1}\Sigma_f^I(\omega) \sim \frac{2}{3}\left[1 + \frac{8}{\pi^2}\ln^2(a|\tilde{\omega}|)\right] \tag{4.3a}$$

$$\Delta_0^{-1}\Sigma_f^R(\omega) \sim -\text{sgn}(\omega)\frac{16}{3\pi}\ln(a|\tilde{\omega}|) \tag{4.3b}$$

for $|\tilde{\omega}| \gg 1$ (or $\gg \max(1, \tilde{T})$ at finite $\tilde{T}$), with a a pure constant $\mathcal{O}(1)$, and hence from equations (3.4) and (4.2) that

$$\pi\Delta_0 D_f(\omega) \sim \frac{1}{\tilde{\tau}(\omega; T)} \overset{|\tilde{\omega}|\gg 1}{\sim} \frac{3\pi^2}{16}\frac{[\ln^2(a|\tilde{\omega}|) + \frac{\pi^2}{8}]}{[\ln^2(a|\tilde{\omega}|) + \frac{\pi^2}{8}]^2 + [\pi\ln(a|\tilde{\omega}|)]^2}. \tag{4.4}$$

In figure 8 for $T = 0$, the $\tilde{\omega}$-dependence of $\tilde{\tau}^{-1}(\omega; 0)$ is shown, for both the BL and HCL. It is also compared directly to equation (4.4). The asymptotics for the two lattices coincide in practice for $|\tilde{\omega}| \gtrsim 5$–10 (as expected e.g. from figure 2). Moreover, the 'high'-energy behaviour of the tails in $\tilde{\tau}^{-1}(\omega; T)$ (or equivalently $\pi\Delta_0 D^f(\omega)$) is indeed seen to be that of equation (4.4) (with the constant $a \sim 0.55$ determined numerically). We also add in passing that the full form equation (4.4) is required for the very good agreement over a wide $\tilde{\omega}$-range evident in figure 8, i.e. it is not exclusively dominated by the ultimate large-$\tilde{\omega}$ asymptotic behaviour $\pi\Delta_0 D^f(\omega) \sim \tilde{\tau}^{-1}(\omega; T) \sim 3\pi^2/[16\ln^2(|\tilde{\omega}|)]$.

Finally, explicit comparison to IPT [10, 21] is made in figure 9, for the $\tilde{\omega}$-dependence of both the $T = 0$ f-electron spectrum $\pi\Delta_0 D^f(\omega)$ and the scattering rate $\tilde{\tau}^{-1}(\omega; 0)$ (again omitting the $\delta(\tilde{\omega})$ contribution). The LMA results shown are naturally the universal scaling forms, independent of the bare model parameters. Corresponding IPT results are again obtained for $U/t_* = 3$ and $V/t_* = 0.25$. The figure illustrates three points.

 (i) IPT does not capture the important logarithmic tails (and hence e.g. produces much reduced scattering rates, even for $T = 0$ considered).
 (ii) Its f-electron spectrum recovers, but amounts to little more than, the limiting low-frequency quasiparticle form (as seen by comparison to figure 2 above).
(iii) The approach does not produce an exponentially small gap scale, and hence a 'clean' separation between low (meaning universal) and high energy scales; e.g. non-universal scales on the order of $\omega \sim 0.1t_*$ are reached by $\tilde{\omega} \sim 50$ in the IPT results shown in figure 9.

We also note that the IPT transport rate $\tilde{\tau}^{-1}(\omega; 0)$ actually vanishes for $|\tilde{\omega}| \leqslant 3\Delta_g$, rather than Δ_g itself. This in turn is related to the spurious behaviour in the T-dependence of the resistivity arising from IPT, that is discussed further in the following section.

5. DC transport

We now consider dc transport properties of the PAM. Our aim here is to understand the temperature dependence of the static conductivity/resistivity, in particular over the full $\tilde{T}$-range in the strong-coupling/Kondo lattice scaling regime, as well as the connection between the high-$\tilde{T}$ behaviour of the PAM and that of the single-impurity Anderson model.

As discussed in section 3, the dc conductivity $\sigma(0; T) = \frac{1}{3}\sigma_0 F_\alpha(0; T)$, with the dimensionless $F_\alpha(\omega; T)$ given respectively for the hypercubic and BLs by equations (3.7a) and (3.7b). In the strong-coupling regime of interest the static conductivity naturally exhibits scaling in $\tilde{T} = T/\Delta_g$, with no dependence on the bare system parameters U, V and t_*. The resultant scaling form does of course depend on the lattice type (cf section 4 for single-particle dynamics), and $F_\alpha(0; T)$ for the two lattices is shown in figure 10. For the HCL the figure also shows (dotted) the $\tilde{T}$-dependence arising from the approximate but physically
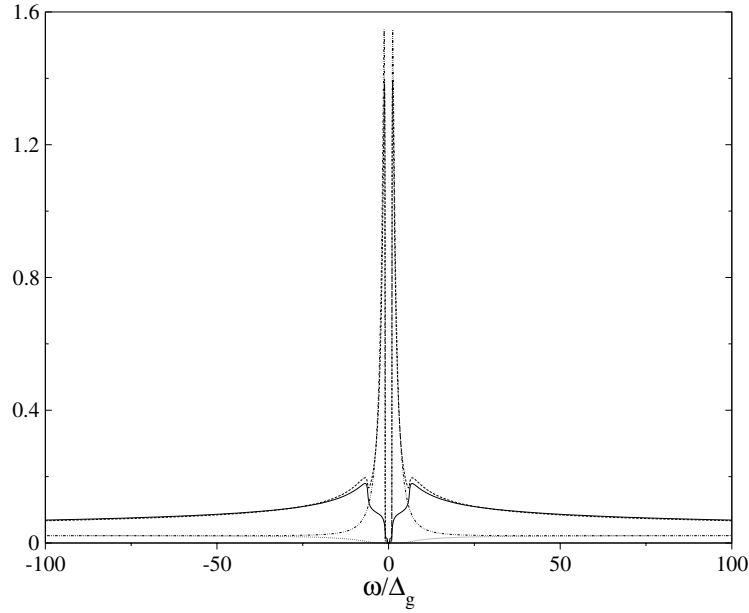
Figure 9. Comparing the ω/Δ_g-dependence of scattering rates and f-electron spectra (BL) arising from the LMA and IPT: $\pi\Delta_0 D^f(\omega)$ (LMA, dashed curve; IPT, double point–dash curve) and $\tilde{\tau}^{-1}(\omega; 0)$ (LMA, solid curve; IPT, dotted curve). The LMA results are naturally universal; IPT results were obtained for $U/t_* = 3$ and $V/t_* = 0.25$.

intuitive form equation (3.10), namely $F_{HCL}(0; T) \propto -\int_{-\infty}^{+\infty} d\omega \frac{\partial f(\omega)}{\partial\omega}\tilde{\tau}(\omega; T)$ with $\tilde{\tau}(\omega; T)$ the (dimensionless) scattering time. Two initial points should be noted here. First that the latter approximation, while qualitatively inadequate as $\tilde{T} \to 0$ where it fails to capture the insulating ground state, is very good for $\tilde{T} \gtrsim 2$ or so; in fact as further evident from the inset to figure 10, where comparison is made up to $\tilde{T} = 200$, it coincides asymptotically, and rapidly, with $F_{HCL}(0; T)$ obtained from the exact equation (3.7a). Second, recalling (section 3) that the constant σ_0 is realistically on the order of $\sim 10^4$–10^5 Ω^{-1} cm^{-1}, we note that the results of figure 10 readily encompass static conductivities $\sigma(0; T)$ on the order of $\sim 10^3$–10^4 Ω^{-1} cm^{-1} that are typical of Kondo insulating materials around room temperature [3–7] (see also section 7).

The insulating nature of the ground state is self-evident in figure 10; and for sufficiently low T one expects and finds activated transport of the form

$$\tilde{\sigma}(0; T) \propto \exp[-\Delta_{tr}/T] \tag{5.1}$$

which defines the transport gap Δ_{tr}. For the BL we find $\Delta_{tr} = \Delta_g$, while for the HCL one naturally finds $\Delta_{tr} \propto \Delta_g$, but with a proportionality constant differing from unity ($\sim$0.4).

We turn now to consider the $\tilde{T}$-dependence of the static conductivity/resistivity over the full $\tilde{T}$-range, for both the HCL and BL; and in addition to compare the resultant behaviour, at high $\tilde{T}$ in particular, to that arising for the AIM. The resistivity for the pure impurity model, $\rho'_{imp}(T) = \rho_{imp}(T)/\rho_{imp}(0)$ with $\rho_{imp}(T)$ the change in resistivity due to addition of the impurity, is given from equation (3.11). To compare like with like in the following, comparison of equation (3.10) for the HCL with equation (3.11) for the AIM suggests that for
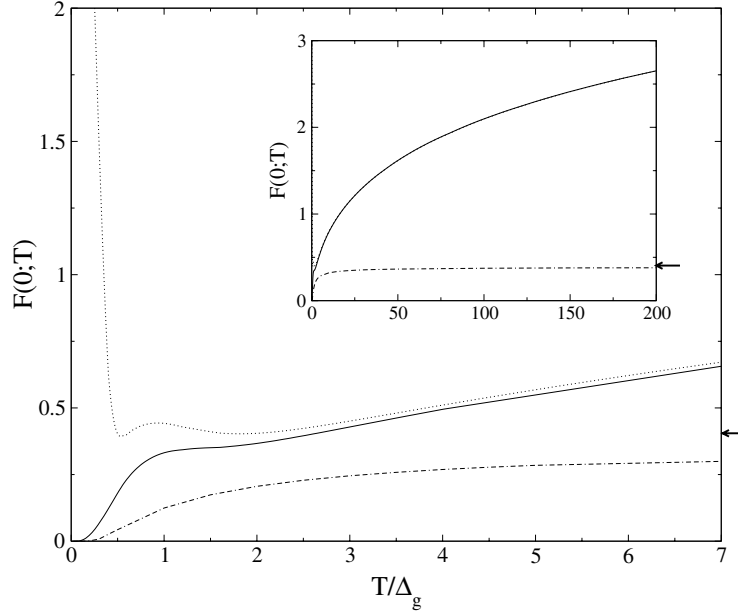
Figure 10. Temperature dependence of the static conductivities in the Kondo lattice scaling regime: $F_\alpha(\omega = 0; T)$ versus $\tilde{T} = T/\Delta_g$ for the HCL (solid curve) and BL (point–dash curve); the approximate equation (3.10) for the HCL is also shown (dotted curve). The high-temperature asymptote for the BL ($4/\pi^2 \simeq 0.4$) is indicated by an arrow. Inset: results on an expanded scale out to $\tilde{T} = 200$.

the HCL we consider the dimensionless resistivity

$$\rho'_{HCL}(T) = \frac{\frac{1}{2}[\rho_0 t_*]^2}{F_{HCL}(0; T)} \equiv \frac{1}{2\pi F_{HCL}(0; T)} \tag{5.2}$$

(the BL counterpart of which is given below, equation (5.4)).

First let us consider the important differences between the hypercubic and BLs, which in turn reveals equally important similarities between the two. From figure 10 it appears that with increasing $\tilde{T}$, $F_{HCL}(0; T)$ is growing apparently unboundedly, albeit relatively slowly, while $F_{BL}(0; T)$ is slowly saturating to a constant value $F_{BL}(0; T) \approx 0.4$. This is indeed the case, and stems from the fact that in the limit of vanishing hybridization $V = 0$—where the f levels decouple from the conduction band—the BL has a non-zero residual ($T = 0$) conductivity/resistivity (in contrast of course to *any* $V > 0$, for which the $T = 0$ conductivity vanishes), specifically, as follows straightforwardly using equation (3.7b), that

$$F_{BL}^{V=0}(0; T = 0) = [\rho_0 t_*]^2 = \frac{4}{\pi^2}. \tag{5.3}$$

It is this, the residual conductivity of the free ($V = 0$) conduction band, that corresponds to the ultimate high-$\tilde{T}$ constant asymptote seen in the inset to figure 10 for the BL ($4/\pi^2 = 0.405\ldots$, marked by an arrow in the figure). This is further evident if one considers the temperature dependence of $F_{BL}(0; T)$ on 'all scales', i.e. versus T/t_*, as shown in figure 11 for a sequence of increasing U/t_* in strong coupling. Here the T/t_*-dependence of $F_{BL}^{V=0}(0; T)$ is also shown, and is seen to constitute an upper bound to the T/t_*-dependence of $F_{BL}(0; T)$ itself. Since the gap Δ_g is exponentially small in strong coupling, the scaling behaviour of $F_{BL}(0; T)$ illustrated in figure 10 for finite $\tilde{T} = T/\Delta_g$ corresponds in figure 11 to exponentially small
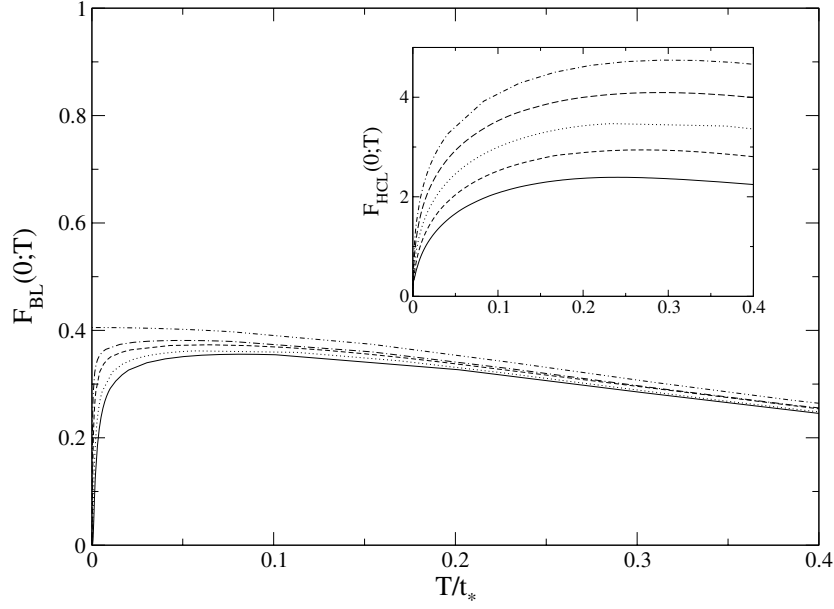
Figure 11. Temperature dependence of static conductivities on 'all scales', versus T/t_*: $F_{BL}(0; T)$ for $V^2/t_*^2 = 0.2$ and $U/t_* = 4.6$ (solid), 5.1 (dotted), 6.1 (dashed) and 7 (point–dash). The $V = 0$ limit $F_{BL}^{V=0}(0; T)$ is also shown (double point–dash). Inset: corresponding results for $F_{HCL}(0; T)$ for $U/t_* = 4.6$ (solid), 5.1 (short dash), 5.6 (dotted), 6.1 (long dash) and 6.6 (point–dash); in this case, $F_{HCL}^{V=0}(0; T) = \infty$.

values of $T/t_* = \tilde{T}\frac{\Delta_g}{t_*}$, whence, as seen from figure 11, $F_{BL}(0; T)$ is bounded above by $F_{BL}^{V=0}(0; T = 0)$ for large $\tilde{T}$ in the scaling regime (which corresponds formally to any finite $\tilde{T}$ in the limit $\Delta_g \to 0$).

The latter behaviour is readily understood in physical terms, since in the scaling regime the gap in the conduction band $D^c(\omega)$ rapidly fills in with increasing $\tilde{T}$ and approaches the free $V = 0$ conduction band (see e.g. figures 4(b) and 5(b)). For $\tilde{T} \gg 1$ the gap Δ_g is thus in essence irrelevant, i.e. might as well be zero—which is of course just the $V = 0$ limit, with its characteristic residual resistivity for the BL. For the HCL by contrast the residual resistivity for $V = 0$ is precisely zero, reflecting the infinite conductivity associated with the coherent Bloch states that in this case arise when $V = 0$. So for the HCL, by the same reasoning, one does not therefore expect the conductivity *in the scaling regime* to saturate for $\tilde{T} \gg 1$, as indeed evident in figure 10 (see also figure 11 (inset) where the T/t_*-dependence of $F_{HCL}(0; T)$ is shown for a sequence of increasing U/t_*, as well as figure 12 below). We believe this conclusion to be rather general: if for whatever reason the free ($V = 0$) conduction band is characterized by a non-vanishing residual conductivity/resistivity, be it due e.g. to the intrinsic nature of the free conduction band or to the presence of disorder, then we expect the conductivity in the scaling regime to approach asymptotically this limiting value for $\tilde{T} \gg 1$.

To take the above into account when comparing the two lattices it is natural to subtract from the resistivity any finite high-$\tilde{T}$ asymptote, as embodied in $1/F_\alpha(0; T) - 1/F_\alpha^{V=0}(0; 0)$ (a redundant operation for the HCL where $F_{HCL}^{V=0}(0; 0) = \infty$); considering therefore—in obvious parallel to the AIM—the 'change in resistivity due to coupling the f levels to the host conduction
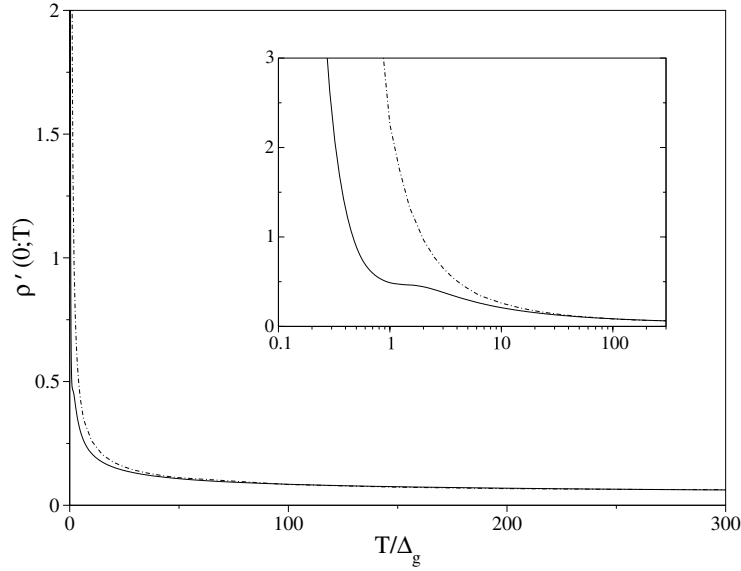
Figure 12. Resistivities in the Kondo lattice scaling regime: $\rho'_{HCL}(T)$ (equation (5.2), solid curve) and $\rho'_{BL}(T)$ (equation (5.4), point–dash curve) versus $\tilde{T} = T/\Delta_g$. Inset: same results on a logarithmic $\tilde{T}$ scale.

band'. Specifically, for the BL we consider below the following dimensionless resistivity:

$$\rho'_{BL}(T) = \frac{F_{BL}^{V=0}(0; 0)}{F_{BL}(0; T)} - 1 \equiv \frac{4}{\pi^2 F_{BL}(0; T)} - 1. \tag{5.4}$$

We have just highlighted the differences between the HCL and BL. But their important similarities are evident in figure 12, where we show the resultant scaling behaviour of the resistivities $\rho'_{HCL}(T)$ (equation (5.2)) and $\rho'_{BL}(T)$ (equation (5.4)) as a function of $\tilde{T} = T/\Delta_g$ out to $\tilde{T} \simeq 300$; the inset shows the same results on a log scale, indicating that the $\rho'(T)$ ultimately vanish as $\tilde{T} \to \infty$. Two immediate features are apparent. The first is that the high-$\tilde{T}$ asymptotics of the $\rho'(T)$ coincide (whence re figure 10, the rate at which the BL conductivity $F_{BL}(0; T)$ asymptotically approaches its saturation value is the same as that with which its HCL counterpart grows unboundedly); the leading asymptotics is obtained explicitly below. In fact, for $\tilde{T} \gtrsim$ 5–10 or so, the behaviour of the two lattices is barely distinguishable. Second, cursory inspection of figure 12 might suggest that the resistivities $\rho'(T)$ are themselves plateauing with increasing $\tilde{T}$, since they change only slightly over a large temperature range out to many multiples of the gap. This interpretation, while rather natural at first sight, is not correct since the $\rho'(T) \to 0$ as $\tilde{T} \to \infty$. But it is indicative of the very slow $\tilde{T}$-decays involved; and for which, see section 7, we believe there is experimental evidence in Kondo insulating materials.

We now obtain the leading high-$\tilde{T}$ behaviour of the $\rho'(T)$, here considering explicitly $\rho'_{HCL}(T)$. Precisely the same result (equation (5.8) below) is obtained for $\rho'_{BL}(T)$, which separate calculation is outlined in the appendix. From equation (5.2) together with equation (3.10) (which is asymptotically valid at large-$\tilde{T}$ as illustrated in figure 10),

$$\frac{1}{\rho'_{HCL}(T)} \sim - \int_{-\infty}^{\infty} d\omega \, \frac{\partial f(\omega; T)}{\partial \omega} \tilde{\tau}(\omega; T) \tag{5.5}$$

where the scattering time $\tilde{\tau}(\omega; T)$ is given by equation (3.4) in terms of the f-electron self-energy $\Delta_0^{-1} \Sigma_f(\omega; T)$. The latter is given for $|\tilde{\omega}| \gg \max(1, \tilde{T})$ by equation (4.3), the generalization of which to $\tilde{T} \gg 1$ and any $|\tilde{\omega}|$ (holding also for the BL) is [32]

$$\Delta_0^{-1} \Sigma_f^I(\omega; T) \sim \frac{16}{3\pi^2} \ln^2 \left[a \sqrt{|\tilde{\omega}|^2 + (\pi \tilde{T})^2} \right] \tag{5.6}$$

with $\Delta_0^{-1} \Sigma_f^R(\omega; T) \propto [\Delta_0^{-1} \Sigma_f^I(\omega; T)]^{1/2}$ (such that it may be neglected in equation (3.4) for the scattering time). Equation (3.4) thus yields

$$\tilde{\tau}(\omega; T) \sim \Delta_0^{-1} \Sigma_f^I(\omega; T) \sim \frac{16}{3\pi^2} \ln^2(\tilde{T}) L(y; \tilde{T}) \tag{5.7}$$

where $y = \tilde{\omega}/\tilde{T}$, and $L(y; \tilde{T}) = [1 + \ln[a\sqrt{\pi^2 + y^2}]/\ln(\tilde{T})]^2$ such that $L(y; \tilde{T}) \to 1$ as $\tilde{T} \to \infty$ for finite y. Using equation (5.7) in (5.5), and changing variables therein from ω to y, gives directly the leading high-$\tilde{T}$ behaviour of $\rho'_{HCL}(T)$ as

$$\rho'(T) \overset{\tilde{T} \gg 1}{\sim} \frac{3\pi^2}{16 \ln^2(\tilde{T})} \tag{5.8}$$

(which as above also holds for $\rho'_{BL}(T)$, see the appendix).

Equation (5.8) reflects the anticipated connection between the PAM at high $\tilde{T}$ and the AIM, being also the exact high-temperature asymptote for the strong-coupling AIM (with Kondo temperature $\propto \Delta_g$) [2], first obtained [42] for the Kondo model from the leading logarithmic sum of parquet diagrams. That connection is seen more generally in figure 13, where the full temperature dependence of the HCL resistivity is compared directly to corresponding LMA results for the AIM (analogous comparison for the BL is clear from figure 12). Specifically, we show $\rho'_{HCL}(T)$ versus $\tilde{T} = T/\Delta_g$ (with $\Delta_g = ZV^2/t_* \equiv \Delta_0 Z/\sqrt{\pi}$), compared to the impurity resistivity $\rho'_{imp}(T) = \rho_{imp}(T)/\rho_{imp}(0)$ versus $\tilde{T} = T/\Delta_g^{imp}$ (where $\Delta_g^{imp} \equiv \Delta_0 Z_{imp}/\sqrt{\pi}$ with Z_{imp} the AIM quasiparticle weight). The LMA $\rho'_{imp}(T)$ is detailed in [32] where it is shown to agree rather well with NRG calculations for the AIM [43], to be asymptotically exact at high $\tilde{T}$ (equation (5.8) being recovered), to agree well with the Hamann approximation [44] (obtained by further parquet resummation) in the latter's regime of applicability down to $\tilde{T} \sim 1$ and to cross over smoothly to the AIM Fermi liquid form $\rho'_{imp}(T) - 1 \propto -\tilde{T}^2$ as $\tilde{T} \to 0$. As evident in figure 13 the PAM resistivity $\rho'_{HCL}(T)$, which exhibits activated insulating behaviour (equation (5.1)) for $\tilde{T} \lesssim 0.5$ or so, progressively diminishes with increasing $\tilde{T}$ and for $\tilde{T} \gtrsim 1$–2 essentially coincides with that for the AIM.

The above results are in marked contrast to those arising from IPT [10, 21], the behaviour of which is qualitatively wrong. IPT results for $\rho'_{HCL}(T)$ versus $\tilde{T}$ are compared to the LMA in the inset to figure 13. The IPT calculations were performed for $U/t_* = 3$ and $V/t_* = 0.25$ (as employed for the BL in section 4.1), and the inability of IPT to recover an exponentially small gap scale means that non-universal temperatures on the order of $T \sim 0.1 t_*$ are reached by $\tilde{T} \sim 60$. It is evident from figure 13 that the IPT resistivities are generally much less than their LMA counterparts, and no hint of logarithmic $\tilde{T}$-decays is evident (which mirrors the absence of logarithmic tails in the $\tilde{\omega}$-dependence of the IPT single-particle spectra and scattering rates, section 4). Most significantly, however, we see that the IPT resistivity actually *vanishes* as $\tilde{T} \to 0$, rather than exhibiting the correct divergence symptomatic of the insulating ground state. At first sight this is surprising, since IPT is qualitatively correct in predicting a $T = 0$ gap in the single-particle spectra $D^{c/f}(\omega)$ [10, 21]; we have thus examined the problem in some detail. Its physical origins stem from the fact that the imaginary part of the IPT $T = 0$ self-energy, $\Sigma_f^I(\omega; 0)$, is zero for $|\omega| < 3\Delta_g$ rather than for $|\omega| \lesssim \Delta_g$ as one might expect (where 'zero' strictly means exponentially small for the HCL with its soft gap,
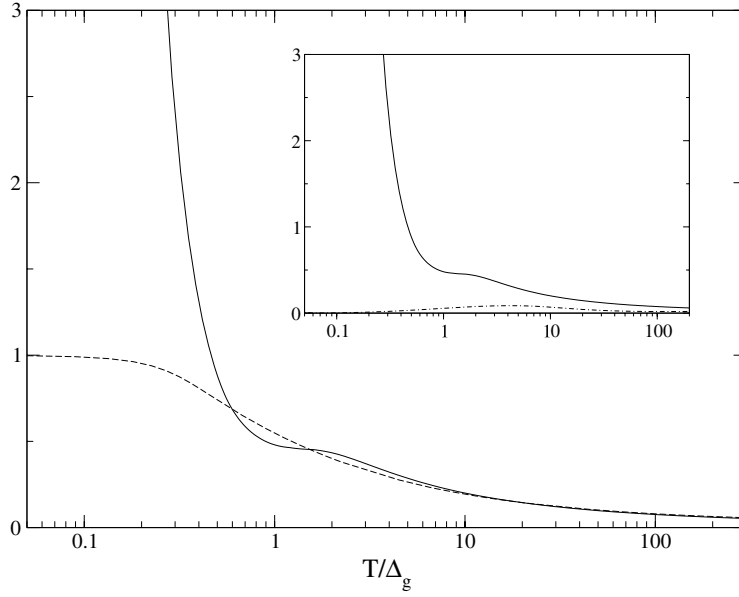
Figure 13. Comparison of resistivities for the HCL and AIM: $\rho'_{HCL}(T)$ (solid curve) and $\rho'_{imp}(T)$ (dashed curve) versus $\tilde{T} = T/\Delta_g$ on a log scale. Inset: comparison of $\rho'_{HCL}(T)$ arising from the LMA (solid curve) and IPT (point–dash curve).

although that is irrelevant in the following); and in consequence the scattering rate $\tau^{-1}(\omega; 0)$ (see equation (3.4)) likewise vanishes for $0 < |\omega| < 3\Delta_g$. But for $|\omega| \gtrsim \Delta_g$, there is a high density of conduction electron states embodied in $D^c(\omega)$ (see e.g. figures 2 or 4). Hence, states in the interval $\Delta_g \lesssim |\omega| \lesssim 3\Delta_g$ are essentially *unscattered*; and it is this that, on initially increasing T from zero (and thus accessing states in this interval), leads to an arbitrarily large conductivity and hence vanishing of $\rho'_{HCL}(T)$ as $T \to 0$. This can be demonstrated numerically in several ways (e.g. by 'cutting off' the Fermi functions $\partial f(\omega; T)/\partial\omega$ entering $\rho'_{HCL}(T)$ in the above $|\omega|$ interval); but the physical argument above is the basic origin of the problem. This spurious behaviour does not arise within the LMA, for which $\Sigma^I_f(\omega; 0)$ and the single-particle spectra are non-vanishing in the *same* $|\omega|$ intervals. The problem can be circumvented within IPT by *ad hoc* addition of a finite η in frequency factors $\omega^+ = \omega + i\eta$ (to mimic an additional white-noise inelastic scattering rate), as has been employed in a weak-coupling IPT study [45]. In this case, we find the ultimate low-T behaviour of the resistivity to be of the form $\rho'_{HCL}(T) \sim \eta \exp(b\Delta_g/T)$ (with $b \sim 0.4$), but with a crossover temperature scale to activated behaviour that is entirely determined by η and vanishes as $\eta \to 0$.

6. Optical conductivities

The natural progression is now to consider the optical conductivities $\sigma(\omega; T) = \frac{1}{3}\sigma_0 F_\alpha(\omega; T)$, with the $F_\alpha(\omega; T)$ given explicitly for the hypercubic and BLs by equations (3.7). Before proceeding to specific results arising from the LMA, we consider a basic question regarding the optical gap: what is it? While strictly an issue at $T = 0$ since all gaps are technically destroyed for $T > 0$, this of course has major ramifications for both the frequency and temperature dependence of the optical conductivity.

We note at the outset that our most basic conclusion here differs qualitatively from the work of [21]. It has been argued hitherto (see e.g. figure 2 of [21]) that the optical gap in $\sigma(\omega; 0)$ corresponds to the minimum *direct gap* Δ_{dir} of the renormalized band structure, as opposed to the *indirect gap* $\Delta_{ind} \propto \Delta_g = ZV^2/t_*$ that is manifest in the single-particle spectra $D^c(\omega)$ or $D^f(\omega)$; a conclusion that in turn underpins the interpretation of experiment given in [21] (see also [6]). We do not believe this to be correct on general grounds, neither do we find it supported by the present theory. By contrast we show, in agreement with the qualitative conclusions of [7], that

(i) the optical gap corresponds to the indirect gap (albeit that the direct gap scale is obviously also manifest in the ω-dependence of the optical conductivity) and

(ii) it is the indirect gap which sets the temperature scale for the thermal evolution of the optical conductivity in the Kondo lattice regime, in particular the 'filling' of the optical gap with increasing temperature (which we regard as entirely natural, since in strong coupling Δ_g is the characteristic low-energy scale of the system).

It is first necessary to explain why we disagree in particular with the conclusions of [21]. As discussed in section 2.1 (see also [2, 10, 36]) the limiting low-frequency behaviour of the single-particle Green functions amounts to a renormalization of the non-interacting limit, arising from the exact equations (2.5) by neglecting the imaginary part of the f-electron self-energy $\Sigma_f^I(\omega; 0)$ and replacing $(\text{Re}\,\Sigma_f(\omega; 0) \equiv)\,\Sigma_f^R(\omega; 0)$ by its leading low-ω behaviour, namely

$$\Sigma_f(\omega; 0) \sim \Sigma_f^R(\omega; 0) \sim -\left(\frac{1}{Z} - 1\right)\omega \tag{6.1}$$

with Z the quasiparticle weight. This leads directly to the quasiparticle behaviour embodied in equations (2.20), e.g. $G^c(\omega) \sim g_0^c(\omega; ZV^2)$ with $g_0^c(\omega; V^2)$ referring to the $U = 0$ limit, whence the lowest-ω behaviour of $D^c(\omega)$ (and likewise $D^f(\omega)$) is a simple quasiparticle renormalization of the non-interacting limit, with $V^2 \to ZV^2$. In particular (section 2.1) the gap in the single-particle spectra is generically preserved. This is the indirect gap scale defined by

$$\Delta_{ind} = 2\Delta_g = 2Z\frac{V^2}{t_*} \tag{6.2}$$

which is indeed manifest in the single-particle spectra (the 2 simply reflecting the 'full' gap, as opposed to that measured from the Fermi level at mid-gap, $\omega = 0$). The quasiparticle form for the single-particle propagators is not approximate: it must be satisfied asymptotically at sufficiently low frequencies, reflecting as it does Fermi liquid behaviour in the sense of adiabatic continuity to the non-interacting limit; and indeed it is, as illustrated in figure 2 (see also [36]). We emphasize however that this quasiparticle behaviour is confined to the lowest frequency scales $|\tilde{\omega}| = |\omega|/\Delta_g$, up to at most a few times the (indirect) gap $\Delta_g \propto Z$, beyond which, as detailed in section 4 and [36], this simple picture no longer holds.

The arguments above may be extended—but with a wholly different validity—to the optical conductivity; it is this that underlies the conclusion of [21]. From equations (3.7), the optical conductivities are determined by the $D_c(\epsilon; \omega) = -\frac{1}{\pi}\,\text{Im}\,G^c(\epsilon; \omega)$, where (section 3) $G^c(\epsilon; \omega) = [\gamma(\omega) - \epsilon]^{-1}$ with $\gamma(\omega) = \omega^+ - V^2[\omega^+ - \Sigma_f(\omega; T)]^{-1}$. If the asymptotic form equation (6.1) for $\Sigma_f(\omega; 0)$ is again employed here, then $\gamma(\omega) \approx \omega^+ - \frac{ZV^2}{\omega^+}$ and hence $G^c(\epsilon; \omega) \approx [\omega^+ - \frac{ZV2}{\omega^+} - \epsilon]^{-1}$ which again amounts to a renormalization of the non-interacting limit. The two branches characteristic of this renormalized band structure then follow from the zeros of the approximate $[G^c(\epsilon; \omega)]^{-1}$, being given by $\omega_\pm(\epsilon) = \frac{1}{2}[\epsilon \pm \sqrt{\epsilon^2 + 4ZV^2}]$, with

the ϵ-dependent gap function $\Delta_d(\epsilon) = \omega_+(\epsilon) - \omega_-(\epsilon)$. The minimum such gap occurs for $\epsilon = 0$; this is the (approximate) direct gap,

$$\Delta_{dir} \simeq 2\sqrt{Z}V \tag{6.3}$$

(which, we add in passing, is radically different from the indirect gap equation (6.2) in strong coupling where $Z \ll 1$, since $\Delta_{dir}/\Delta_{ind} \propto Z^{-1/2}$). If now one interprets the optical conductivity of the HCL (given from equation (3.7a)) in terms of a naive picture of renormalized interband transitions, then since Δ_{dir} above corresponds to the minimum energy for such, one would clearly expect it to vanish for $\omega < \Delta_{dir}$; concluding [21] therefore that the optical gap coincides with the direct gap, while the indirect gap is by contrast manifest only in the single-particle spectra, see e.g. figure 2 of [21]. Indeed, if the above approximation $G^c(\epsilon; \omega) \approx [\omega^+ - \frac{ZV^2}{\omega^+} - \epsilon]^{-1}$ is used explicitly in equation (3.7a), one finds directly that $F_{HCL}(\omega; 0) = 0$ for all $\omega \leqslant \Delta_{dir} = 2\sqrt{Z}V$ (and in fact likewise for $F_{HCL}(\omega; T)$ at any T).

The above argument is certainly correct for the *non-interacting* limit of the PAM, which is characterized strictly by simple one-electron states. Despite its superficial appeal, however, it is incorrect beyond the confines of this limit: for it neglects completely [7] the effects of scattering arising from electron interactions, as embodied in the scattering rates $\tau^{-1}(\omega; T) \equiv \gamma_I(\omega)$ (equation (3.3)) considered explicitly in section 4.1, or equivalently (see equation (3.4)) in the imaginary part of the f-electron self-energy $\Sigma_f^I(\omega; T)$, which also controls the single-particle dynamics (sections 2, 4). The effect of this many-body scattering on the optical conductivity may be inferred from equation (3.7a), from which it is straightforward to prove that if $\Sigma_f^I(\omega; 0)$ is non-zero for $|\omega| > \lambda$, then $F_{HCL}(\omega; 0)$ is non-zero for $\omega > 2\lambda$. But the scale λ above which $\Sigma_f^I(\omega; 0)$ effectively (HCL) becomes non-zero is of course the single-particle gap scale Δ_g, whence (equation (6.2)) the optical gap corresponds to the *indirect* gap Δ_{ind}. Four further points should be noted here.

(a) We emphasize that this qualitative conclusion is not dependent on the LMA, although the latter indeed gives $\lambda \sim \Delta_g$. In fact, it also arises within IPT, for which, as discussed in section 5, $\Sigma_f(\omega; 0)$ is non-vanishing for $|\omega| \gtrsim 3\Delta_g$ (the central point again being that $\lambda \propto \Delta_g$).

(b) The above conclusion is certainly consistent (section 5) with a transport gap (equation (5.1)) $\Delta_{tr} \sim \Delta_g$ in the static conductivity: the latter is simply the $\omega = 0$ limit of the optical conductivity, and at the very least it is natural to expect the optical gap to be proportional to the low-temperature gap scale for static transport.

(c) Recall that the scaling regime characteristic of the strong-coupling Kondo lattice (where the quasiparticle weight $Z \to 0$) corresponds to any finite $\tilde{\omega} = \omega/\Delta_g$ in the formal limit $\Delta_g \propto Z \to 0$. But if the optical gap corresponded to the direct gap equation (6.3), this would require $\Sigma_f^I(\omega; 0) = 0$ for all $|\omega| \leqslant \Delta_{dir} \propto Z^{1/2}$. Since such a frequency range clearly encompasses (and goes well beyond) the $\tilde{\omega}$-scaling regime, this would entail *vanishing* scattering rates throughout the scaling regime, which is physically untenable.

(d) Our discussion of the optical gap has in large part focused implicitly on $F_{HCL}(\omega; 0)$ for the HCL. But the same conclusion arises (essentially trivially) for the BL $F_{BL}(\omega; 0)$: from equation (3.7b)

$$F_{BL}(\omega; 0) = \frac{t_*^2}{\omega} \int_{-\omega}^{0} d\omega_1 \, D^c(\omega_1) D^c(\omega_1 + \omega) \tag{6.4}$$

where, since (section 4) the conduction electron spectrum has a gap Δ_g (measured from the Fermi level), the optical gap follows immediately as $\Delta_{ind} = 2\Delta_g$. This suggests in addition that we should expect the optical properties of the HCL and BL to be qualitatively
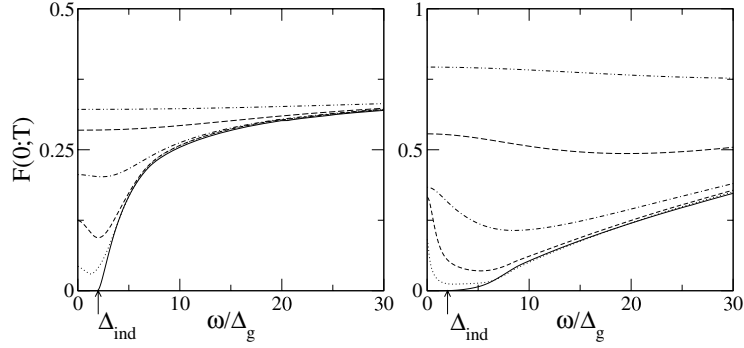
Figure 14. Optical conductivities in the scaling regime: $F_{BL}(\omega; T)$ (left) and $F_{HCL}(\omega; T)$ (right) versus ω/Δ_g for $\tilde{T} = T/\Delta_g = 0$ (solid), 0.5 (dotted), 1 (short dash), 2 (point–dash), 5 (long dash) and 10 (double point–dash). The optical gap $\Delta_{ind} = 2\Delta_g$ is indicated in each case.

similar, at least for sufficiently low frequencies and/or temperatures. That is indeed the case, as we show below.

Figure 14 shows the resultant LMA optical conductivities $F_\alpha(\omega; T)$ (equations (3.7)) for both the BL and HCL, as a function of $\tilde{\omega} = \omega/\Delta_g$ and for a range of temperatures $\tilde{T} = T/\Delta_g$. These are the universal forms, scaling in terms of $\tilde{\omega}$ and $\tilde{T}$ with no dependence on bare material parameters (and by way of orientation we add that, for gaps Δ_g in the range $\sim$10–300 K, $\tilde{\omega} = 30$ would correspond to frequencies ω in the range $\sim$200–6000 cm^{-1}). The indirect gap Δ_{ind} ($=2\Delta_g = 2ZV^2/t_*$) is marked on the figures and is indeed seen to be the ($T = 0$) optical gap. The $T = 0$ optical conductivity is 'sharper' in an obvious sense for the BL than the HCL, but in either case it is again the indirect gap that sets the scale for thermal destruction of the gap: by $\tilde{T} = T/\Delta_g \gtrsim 5$ or so, the gap is well filled in and the optical conductivity essentially constant over the $\tilde{\omega}$-range shown. These are of course characteristic features of experimental Kondo insulators [3–7], as discussed for specific materials in section 7. Here we simply add that $F_\alpha(\omega; T)$ on the order of $\sim$0.25–0.75 lead to absolute conductivities $\sigma(\omega; T) = \frac{1}{3}\sigma_0 F_\alpha(\omega; T)$ in the range $\sim$2500–7500 Ω^{-1} cm^{-1} (taking a typical σ_0 (section 3) of $\sim$3 $\times$ 10^4 Ω^{-1} cm^{-1}): values that are typical for Kondo insulators around room temperature [3–7].

Figure 14 also shows that, on initially increasing $\tilde{T}$ from zero, the optical conductivity acquires a Drude-like peak centred on $\omega = 0$, which broadens with increasing $\tilde{T}$ and is subsequently destroyed as the gap is filled in, as also seen in a QMC study of the HCL [15] (discussed further below). This is more clearly evident in figure 15, where the thermal evolution of the Drude peak for the HCL is shown for $\tilde{T} = 0.4$, 0.8 and 1.2. The figure also makes comparison to a Lorentzian form for the Drude peaks, the quality and range of which fit (and it is merely that) are self-evident.

The optical conductivities shown in figure 14 refer to the universal $\tilde{\omega}$-regime. To consider all ω-scales, encompassing in particular frequencies on the order of the direct gap and beyond, bare model parameters must of course be specified. Figure 16 provides an example, for $U/t_* = 6$ and $V^2/t_*^2 = 0.2$. For both the HCL and BL the optical conductivities $F_\alpha(\omega; T)$ are shown for all ω over which $F_\alpha(\omega; T)$ is non-zero, as a function of $\tilde{\omega} = \omega/\Delta_g$ on a log scale from 10^{-1} to 10^4, and for the same range of temperatures $\tilde{T} = T/\Delta_g$ (up to 10) employed in figure 14. The insets in each case show the renormalized band structure $\tilde{\omega}_\pm(\epsilon) = \omega_\pm(\epsilon)/\Delta_g$ versus the free ($V = 0$) conduction band energies ϵ/t_*; with the branches $\omega_\pm(\epsilon)$ obtained from solution of (Re $\gamma(\omega) \equiv) \gamma_R(\omega) = \epsilon$. From this the fiducial direct gap Δ_{dir} is obtained (occurring
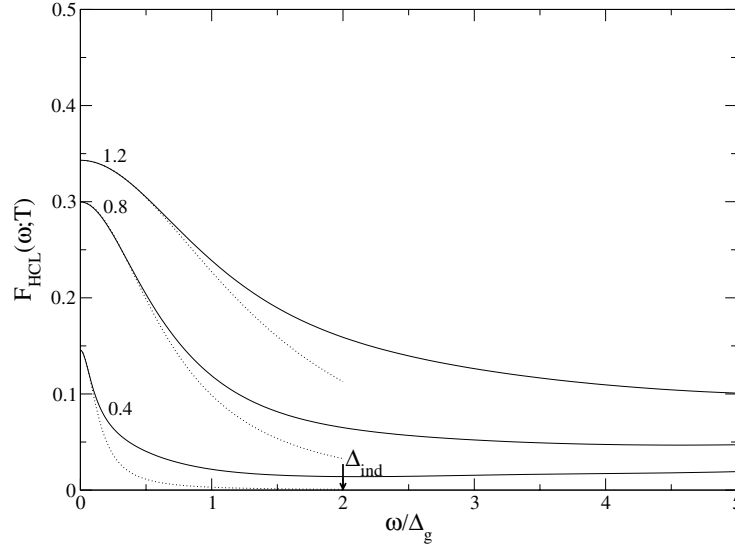
Figure 15. Drude-like peaks in the low-$(\tilde{\omega}, \tilde{T})$ optical conductivity: $F_{HCL}(\omega; T)$ versus ω/Δ_g for $\tilde{T} = T/\Delta_g = 0.4$, 0.8 and 1.2. Lorentzian fits to the data (dotted curves) are also shown.

as expected for $\epsilon = 0$); it is indicated on the frequency axis, and for the particular chosen bare parameters is seen in either case to be $\sim 10^2$ times the indirect gap Δ_{ind} ($= 2\Delta_g$), or $\sim 0.05t_*$. Two features are immediately apparent in figure 16. First, unsurprisingly, the optical conductivity is large on frequency scales on the order of the direct gap; particularly for the HCL where, as expected physically and known from previous work [15, 21], $F_{HCL}(\omega; T)$ is strongly peaked around $\omega \sim \Delta_{dir}$.

The second point concerns the thermal evolution of the optical conductivity. The $\tilde{T} = T/\Delta_g$ range shown in figure 16 corresponds to temperatures up to five times the *indirect* gap $\Delta_{ind} = 2\Delta_g$; over which range, as shown in figure 14, the optical gap 'fills in'. As seen from figure 16, however, temperatures of this order have essentially no effect on the optical conductivity at frequency scales on the order of the direct gap $\Delta_{dir} \sim 10^2 \Delta_{ind}$, which for all practical purposes retain their $T = 0$ values. This is not surprising, for one should expect the optical conductivity on frequency scales $\omega \sim \Delta_{dir}$ to be thermally eroded only on temperature scales of the same order. This is indeed the case, as illustrated in figure 17 which (for the same bare parameters) shows the thermal evolution of $F_{HCL}(\omega; T)$ up to temperatures $\tilde{T} = 200$ (i.e. $T \sim 0.7\Delta_{dir}$): significant thermal erosion on the direct gap scale sets by around $T/\Delta_{dir} \sim 0.1$–0.3, and is well established at the highest temperature shown in the figure.

It is clear from the above that the indirect and direct gap frequency scales, each determined by but with their different dependences upon the quasiparticle weight Z (equations (6.2) and (6.3)), are qualitatively distinct in the strong-coupling Kondo lattice regime where $Z \ll 1$; as too in consequence are the corresponding temperatures for which dynamics on these respective scales evolve. But this 'clean' separation of scales will not of course be evident in the (ω, T)-dependences of the optical conductivity if one is e.g. restricted technique-wise either to low interaction strengths (where $Z \sim \mathcal{O}(1)$) or to high temperatures. This is the case with QMC, and is we believe the reason why the above scale separation is not apparent in the QMC work of [15]. This lack of scale separation is also intrinsic to IPT [21], since its resultant quasiparticle weight decays algebraically rather than exponentially in the interaction
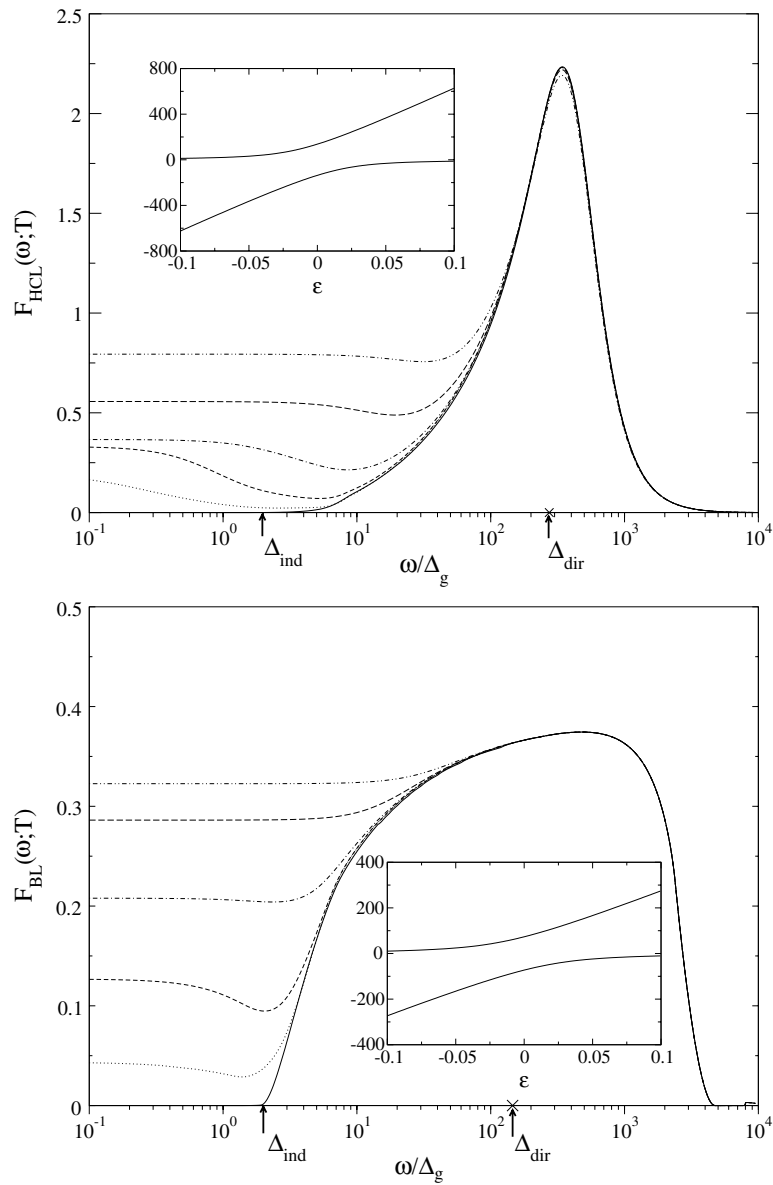
Figure 16. Optical conductivities on all ω-scales: $F_{HCL}(\omega; T)$ (top panel) and $F_{BL}(\omega; T)$ (lower panel) versus ω/Δ_g on a log scale, for $\tilde{T} = T/\Delta_g = 0$ (solid), 0.5 (dotted), 1 (short dash), 2 (point–dash), 5 (long dash) and 10 (double point–dash). The indirect and direct gap scales are also indicated. Temperatures in the range shown produce essentially no effect at ω on the order of the direct gap scale Δ_{dir}. Insets: renormalized band structure $\omega_\pm(\epsilon)/\Delta_g$ versus the free ($V = 0$) conduction band energies ϵ/t_*.

strength. NRG calculations [12, 13] by contrast are not constrained in the above sense, although NRG calculations of finite-T dynamics and transport properties of the PAM have not to our knowledge been performed thus far.
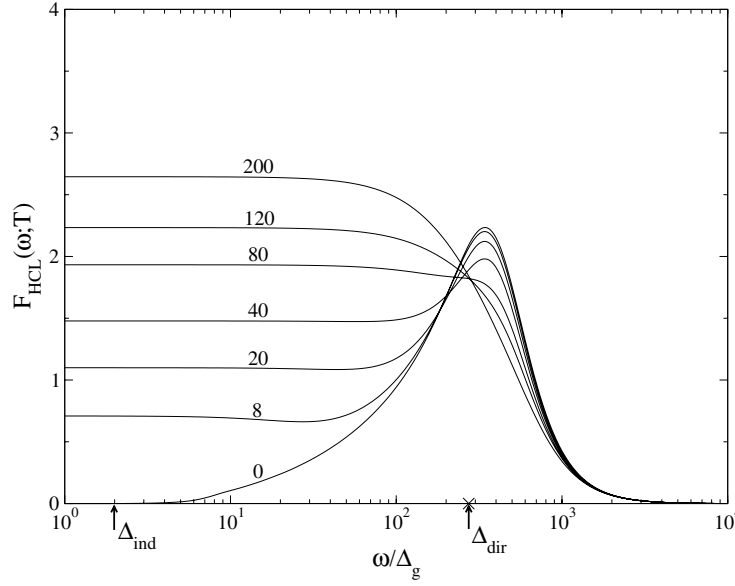
Figure 17. For the same strong coupling parameters as figure 16, $F_{HCL}(\omega; T)$ versus ω/Δ_g for a much wider range of temperatures $\tilde{T} = T/\Delta_g$ up to 200 (i.e. $T/\Delta_{dir} \sim \mathcal{O}(1)$); significant thermal erosion on the direct gap ω-scale occurs only for temperatures of the same order.

7. Experiment

Experimentally, Kondo insulators have been widely studied via an impressive range of techniques (for reviews see e.g. [3–7]). Here we consider briefly three prototypical materials among those for which the most extensive and reliable data is available, namely $Ce_3Bi_4Pt_3$, SmB_6 and YbB_{12}. Each naturally possesses features specific to itself, but the well known commonality of behaviour between the different materials is of course the dominant theme [3–7]. Our aim here is simple: to compare the present theory directly to experimental results for dc transport and optical conductivities. We also emphasize that subsequent comparison to experiment does *not* involve multi-parameter fits, or a detailed knowledge of the bare material parameters; and in these terms is minimalist. The essential point of scaling, as detailed in the preceding sections, is that in strong coupling the temperature dependence of transport/optics is encoded in $\tilde{T} = T/\Delta_g$ alone, independently of the bare model parameters. The gap Δ_g ($\propto \Delta_{tr}$) may thus itself be obtained from experiment (as below); given which, the theory then predicts the full T-dependence. The same comment applies to the ω-dependence of the optical conductivity, which in the scaling regime depends only on $\tilde{\omega} = \omega/\Delta_g$ (albeit of course that 'non-universal' ω (section 6) are also accessed experimentally). All this is naturally based on the assumption that the experimental materials are indeed strongly correlated, which we take for granted unless there appear to be experimental hints to the contrary (as we suggest below may be the case for YbB_{12}).

Granted the above, there is one unknown in the theory, namely the constant σ_0 entering the conductivity $\sigma(\omega; T) = \frac{1}{3}\sigma_0 F_\alpha(\omega; T)$ as an overall scale factor (see e.g. equation (3.6)), which, as noted in section 3, should realistically lie in the range $\sim 10^4$–10^5 Ω^{-1} cm^{-1}. In comparing to experiment we take σ_0 as a parameter, which in practice is indeed found to lie in the above range, although even this is not strictly necessary (knowledge of σ_0 may
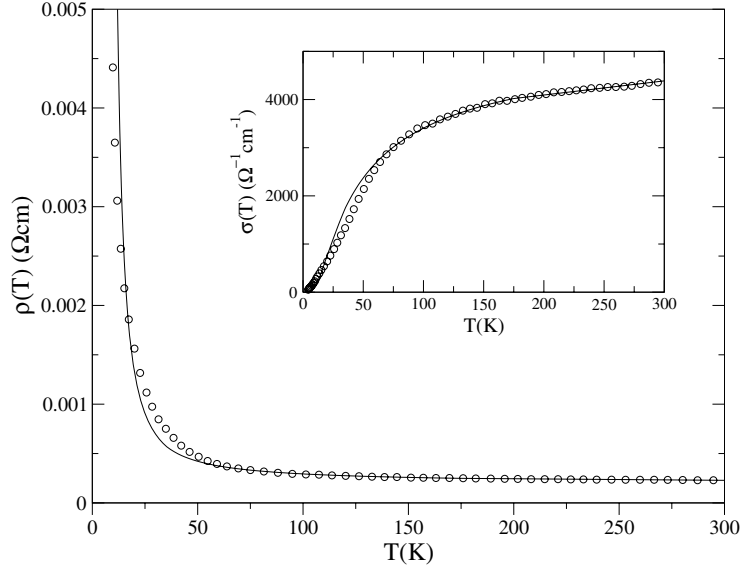
Figure 18. Ce$_3$Bi$_4$Pt$_3$ resistivity $\rho(T)$ (in Ω cm) versus T up to 300 K. Experimental results [46], open circles; theory, solid curve. Inset: corresponding results for the dc conductivity $\sigma(0; T)$.

be bypassed entirely by taking e.g. the room-temperature dc conductivity as a reference and considering $\sigma(\omega; T)/\sigma(0; 300 \text{ K}))$. One must of course choose whether to compare experiment to theoretical results arising from the HCL or BL, the two host lattices we have considered explicitly. Here, we simply make comparison to whichever of the two appears optimal, which in practice means the HCL for all but Ce$_3$Bi$_4$Pt$_3$; a more realistic free ($V = 0$) conduction band density of states $\rho_0(\epsilon)$ could readily be employed, but the comparisons below suggest this would be barely necessary.

7.1. Ce$_3$Bi$_4$Pt$_3$

Experimental results for the resistivity $\rho(T)$ of this classic Kondo insulator are shown in figure 18. These are compared to results arising for $\rho(T)$ ($=1/\sigma(0; T)$) from the present theory for the BL, taking $\sigma_0 \simeq 4.2 \times 10^4 \ \Omega^{-1} \ \text{cm}^{-1}$. The transport gap (equation (5.1)) inferred experimentally is $\Delta_{tr} \simeq 35$ K [46], from which (section 5) $\Delta_g = \Delta_{tr}$ follows.

The quantitative agreement between experiment and theory is clear from figure 18, being excellent for $T \gtrsim 50$ K or so, as seen in particular from the dc conductivity shown directly in the inset. The agreement extends up to $T = 300$ K or $\tilde{T} = T/\Delta_g \sim 10$, an appreciable multiple of the gap where (see e.g. figure 10) the high-temperature logarithmic asymptotics of the Kondo regime are being approached, so that the temperature range shown spans essentially the full range of expected physical behaviour. The activated insulating nature of the low-T transport (equation (5.1)) is likewise evident in the figure, although transport in Ce$_3$Bi$_4$Pt$_3$ at the lowest temperatures is dominated by variable-range hopping between extrinsic states in the gap [46] which the theory does not of course seek to include.

As discussed in section 6, the dc transport and optics should be consistent in the sense that the ($T = 0$) gap in the optical conductivity should correspond to the indirect gap, $\Delta_{ind} = 2\Delta_g$; and the thermal evolution of the optical conductivity should likewise be controlled by the
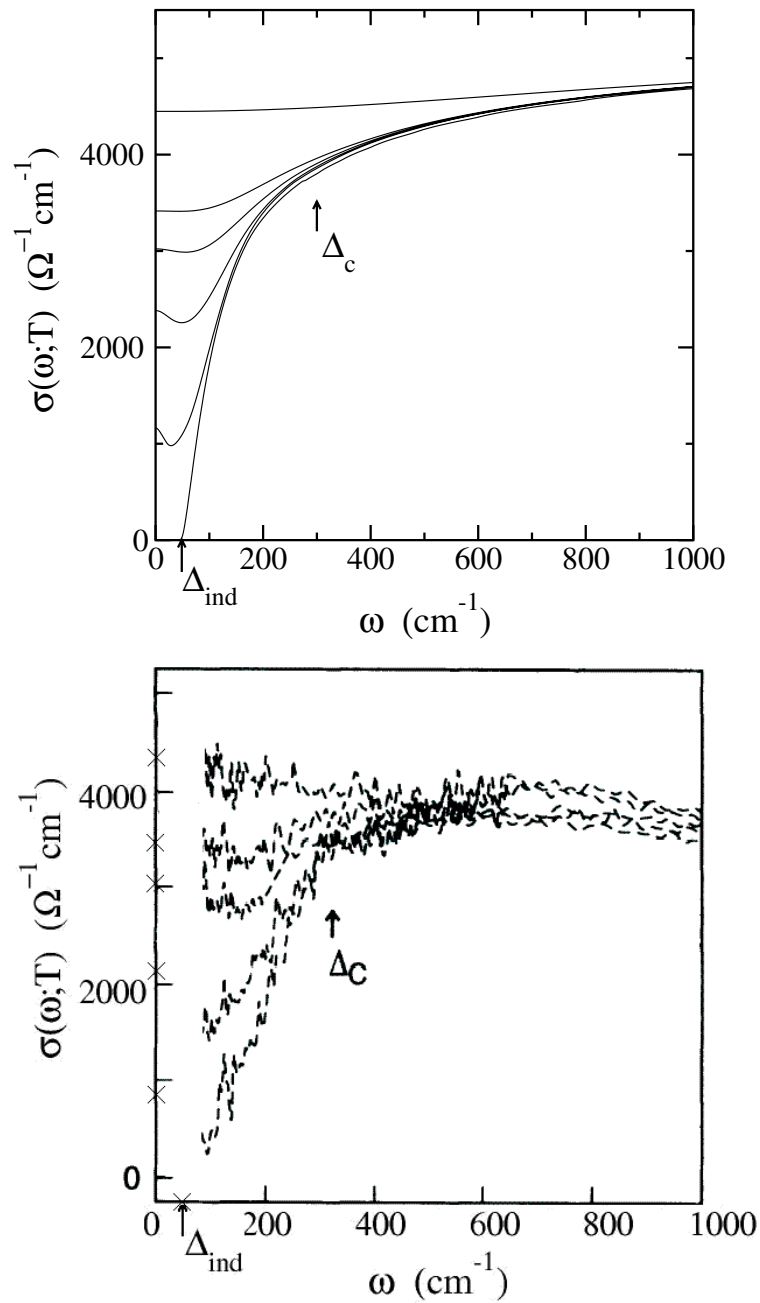
Figure 19. $Ce_3Bi_4Pt_3$ optical conductivity $\sigma(\omega; T)$ (in Ω^{-1} cm^{-1}) versus ω up to 1000 cm^{-1}, and for temperatures $T = 25, 50, 75, 100$ and 300 K (in obvious sequence). Top panel, theory (including $T = 0$); bottom panel, experimental results for $\omega > 50$ cm^{-1} [47], with experimental dc conductivities marked by crosses on the vertical axis. The optical/indirect gap Δ_{ind} is indicated, for 'Δ_c' (see text).

indirect gap scale. Taking $\Delta_{ind} \simeq 70$ K $\simeq 50$ cm^{-1} from the dc experiments as above, figure 19 (top panel) shows the theoretical optical conductivity $\sigma(\omega; T) = \frac{1}{3}\sigma_0 F_{BL}(\omega; T)$ versus ω up to

$1000\,\text{cm}^{-1}$, for temperatures $T = 0, 25, 50, 75, 100$ and $300\,\text{K}$ (each curve thus corresponding to a particular 'realization' of the universal BL optical conductivities shown in figure 10). The lower panel in figure 19 shows corresponding experimental results [47] for $\omega > 50\,\text{cm}^{-1}$, obtained from Kramers–Kronig (KK) transformation of reflectivity measurements; we have also indicated the indirect gap on the ω-axis, and have marked experimental values of the dc conductivity [46] on the vertical axis. The level of agreement between experiment and theory for the optics is self-evident from figure 19, and we regard it as rather good. The relevant temperature scale indeed appears to be the indirect gap [7, 48]: as noted in [47], for T between $100\,\text{K} \sim 1.4\Delta_{ind}$ and $300\,\text{K}$ the optical gap is well filled in and the optical conductivity nearly constant in the far infrared; and the gap begins to develop markedly only below $T \sim 75\,\text{K} \sim \Delta_{ind}$ (which we add is naturally consistent with thermal evolution of the single-particle dynamics, see e.g. figure 4).

As seen from the experimental data in figure 19, the low-temperature dc conductivities are larger than their ac counterparts at the lowest $\omega = 50\,\text{cm}^{-1}$, the difference diminishing with increasing T and being barely perceptible by $T \sim 75\,\text{K} \simeq \Delta_{ind}$. This we believe to be symptomatic of the low-ω Drude-like peak discussed in section 6 (figures 14 and 15), that lies below the detection limit of $50\,\text{cm}^{-1}$ but is apparent (albeit weakly) in the theoretical $\sigma(\omega; T)$, further evidence for which arises in the systems discussed below (see figures 21 and 23). Finally, a remark on the optical gap itself. As noted in [47], linear extrapolation to zero of the steep part of the experimental $\sigma(\omega; T = 25\,\text{K})$ would suggest a gap value on the order of $100\,\text{K}$. This is certainly consistent with $\Delta_{ind} \simeq 70\,\text{K} \simeq 50\,\text{cm}^{-1}$, inferred as above from dc transport. On the other hand, a charge gap $\Delta_c \simeq 300\,\text{cm}^{-1}$ has been identified in [47], for natural reasons evident in the experimental data shown in figure 19 (and with Δ_c indicated on both panels in figure 19). Our point here is simply that Δ_{ind} and Δ_c are fundamentally equivalent scales (each being proportional to the quasiparticle weight Z). The former is 'correct' insofar as the optical gap is strictly a $T = 0$ notion; while the latter is natural if one wishes instead to focus on the incipient development of a gap coming from the 'high'-temperature regime $T \gtrsim \Delta_{ind}$.

7.2. SmB_6

Samarium hexaboride provides another long studied [49], prime example of a Kondo insulator. Here we refer to a recent comprehensive study [50] of both static transport and low-energy electrodynamics, performed on a high-quality single-crystal sample, with the optical conductivity obtained directly via sub-millimetre spectroscopy in the frequency range 5–$36\,\text{cm}^{-1}$ [50], and by KK analysis of reflectivity in the infrared [50, 51]. We restrict our considerations mainly to temperatures $T \gtrsim 8\,\text{K}$, since for lower temperatures variable-range hopping again arises.

Experimental results for the resistivity $\rho(T)$ [50], spanning five orders of magnitude, are shown in figure 20, and compared to theoretical results for the HCL (as one might anticipate to be appropriate for a clean sample), taking $\sigma_0 = 4.7 \times 10^4\,\Omega^{-1}\,\text{cm}^{-1}$ and $\Delta_g = 101\,\text{K}$. Between $T = 8$ and $25\,\text{K}$ the experimental dc conductivity/resistivity has the activated form, equation (5.1), with a transport gap $\Delta_{tr} \simeq 3.5\,\text{meV}\,(\simeq 41\,\text{K})$ [50]. As discussed in section 5, for the HCL we find $\Delta_{tr} = b\Delta_g$ with the constant $b = 0.40$; hence $\Delta_g \simeq 8.75\,\text{meV} \simeq 101\,\text{K}$ as above. The main figure shows $\rho(T)$ on a log scale versus T, while the insets show the corresponding dc conductivity versus both $1/T$ (to exemplify in particular the activated regime) and temperature on a log scale. The agreement between theory/experiment for $T \gtrsim 8\,\text{K}$ is rather striking; for $T \lesssim 8\,\text{K}$ the experimental variable-range hopping behaviour is of course evident from the right-hand inset to the figure.
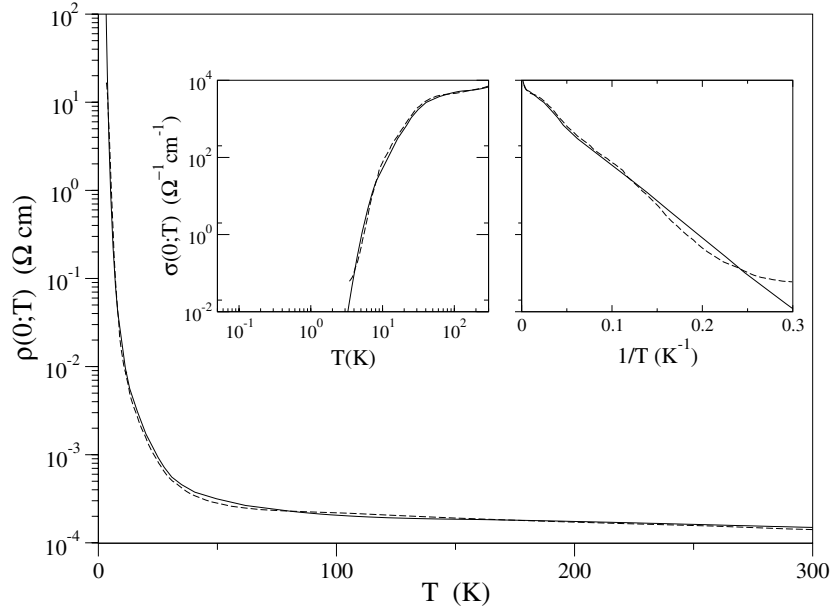
Figure 20. SmB$_6$ resistivity $\rho(T)$ (in Ω cm) versus T up to 300 K. Experimental results [50], dashed curve; theory, solid curve. Left inset: corresponding dc conductivity $\sigma(0; T)$ versus T on a log–log scale. Right inset: $\sigma(0; T)$ on a log scale versus $1/T$; for $T \lesssim 8$ K variable-range hopping arises experimentally.

The consequent optical conductivity $\sigma(\omega; T)$ for the HCL is shown versus ω in figure 21 (top panel) on a log–log scale, for temperatures $T = 3, 13, 16, 18$ and 300 K. Corresponding experimental results for the same temperatures [50] are shown in the lower panel, including the extrapolated conductivities (dashed curves) obtained from the phenomenological fit to the data employed in [50]. The ω-range shown, up to $\sim 3 \times 10^4$ cm^{-1}, naturally encompasses non-universal scales at high frequencies, and the calculations were performed specifically for $U/t_* = 4.5$ and $V^2/t_*^2 = 0.2$. The system is however strongly correlated for these parameters, so we emphasize that the resultant 'low'-ω conductivity (up to ~ 2000 cm^{-1} or so in practice) lies in the $\tilde{\omega} = \omega/\Delta_g$ scaling regime that is actually independent of the bare parameters (sections 4–6): the choice of bare parameters 'matters' only at the high frequency end, and we have simply chosen those above as illustrative. We would however add that for the chosen parameters the quasiparticle weight $Z \sim 5 \times 10^{-3}$, which is in qualitative accord with the experimentally inferred effective mass $(1/Z \sim) m_*/m_0 \sim 10^2$ (from [50]) and $\sim 10^3$ from a previous study [52] (and which values themselves attest to the correlated nature of SmB$_6$).

The first point to note here is that the theoretical optical gap $\Delta_{ind} = 2\Delta_g$, indicated in figure 21, is $\Delta_{ind} \simeq 17.5$ meV $\simeq 200$ K (from Δ_g obtained as above). This accords remarkably well with the gap of 19 ± 2 meV inferred experimentally from the optical conductivity [50], and we emphasize that there is no *a priori* connection between these two ways of obtaining the optical gap—as above, the theoretical optical gap is inferred directly from the much smaller transport gap Δ_{tr}. There is in consequence no conundrum between a transport gap of $\simeq 40$ K and an optical gap of $\simeq 200$ K. The level of agreement between theory/experiment is self-evident in figure 21, and encouraging both in terms of its ω-dependence and thermal evolution. One small twist may also be added. For the phenomenological fitting employed in [50], it was found that for a complete description of the conductivity spectra an additional parameter (termed 'σ_{min}')
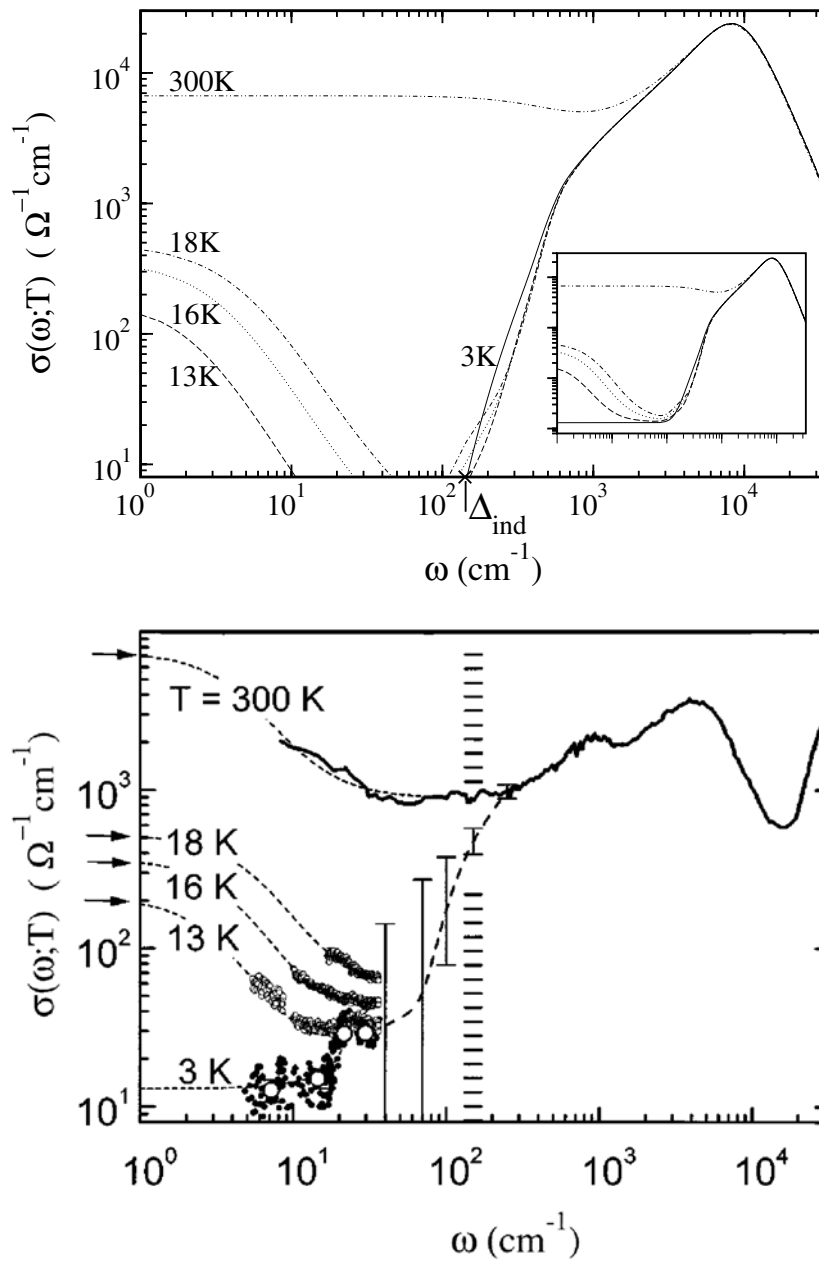
Figure 21. SmB$_6$ optical conductivity $\sigma(\omega; T)$ (in Ω^{-1} cm^{-1}) versus ω on a log–log scale, for temperatures $T = 3, 13, 16, 18$ and 300 K. Top panel: theory (with the theoretical optical/indirect gap indicated). Inset: corresponding results when a constant $12 \, \Omega^{-1}$ cm^{-1} is added. Bottom panel: experimental results [50]. Circles are from sub-mm data [50], solid curves from the reflectivity spectrum via KK [51]. Error bars refer to IR conductivity obtained from KK analysis of the $T = 3$ K reflectivity spectrum assuming 0.5% uncertainty [50]. The shaded area corresponds to the experimental optical gap [50]. The short-dash curves show the extrapolated fit used in [50], and the arrows indicate the experimental dc conductivity.
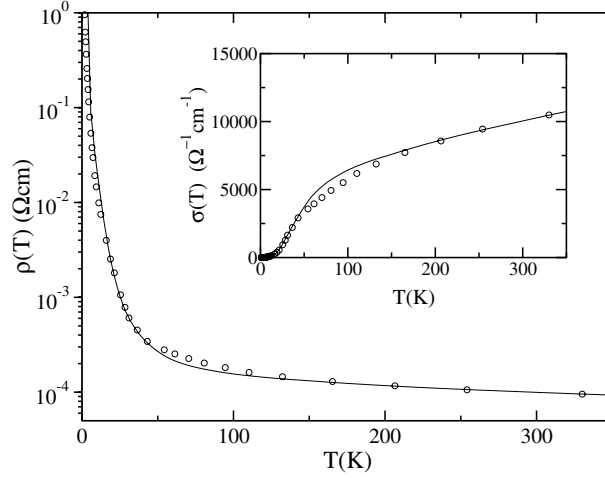
Figure 22. YbB_{12} resistivity $\rho(T)$ (in Ω cm) versus T. Experimental results [53], open circles; theory, solid curve (for parameters specified in text). Inset: corresponding dc conductivities versus T.

had to be introduced in the form of an additive, frequency-independent contribution to the optical conductivity, with $\sigma_{min} \sim 12 \; \Omega^{-1} \; cm^{-1}$ in the low-temperature regime [50]. Without wishing to speculate here on the origin of the σ_{min}, the inset to figure 21 (top panel) shows the effect of simply adding a constant $12 \; \Omega^{-1} \; cm^{-1}$ contribution to our theoretical optical conductivity. For low temperatures its effect is noticeable in the $\sim$10–100 cm^{-1} range, particularly at the lowest $T = 3$ K; and the improved agreement with experiment is clear.

Finally, we mention that we have taken no consideration above of the presence, in the Kondo insulating gap, of an additional narrow donor-type band which is known to occur experimentally [50] in SmB_6 (and may possibly be due to impurities). While certainly of interest in itself, the present theory has of course nothing to say about it; and it plays no role in the extent to which, as above, theory concurs with experiment.

7.3. YbB_{12}

Resistivity [53] and optical measurements [54] have likewise been performed on single-crystal YbB_{12}, the only known Yb-based Kondo insulator. Experimental results for $\rho(T)$ up to $\sim$350 K are shown in figure 22, and for 15 K $< T <$ 40 K exhibit activated behaviour (equation (5.1)) with a transport gap $\Delta_{tr} \simeq 68$ K. Optical conductivity results [54], again obtained via KK from reflectivity spectra combined with a Hagen–Rubens extrapolation at low ω, are shown in the top panel of figure 23. The experimental optical gap is determined as $\Delta_{ind} \simeq 25$ meV $= 290$ K [54], while the strong IR peak around $\sim$0.2–0.25 eV as naturally interpretable [7] in terms of direct gap excitations (see e.g. figures 16, 17 for the HCL).

It is the temperature dependence of the experimental optical data which suggests to us that YbB_{12} may be in an intermediate–weak-coupling regime. As seen from figure 23 [54], increasing temperatures up to $T = 290$ K $\equiv \Delta_{ind}$ leads to significant redistribution of spectral weight at much higher energy scales on the order of the direct gap and beyond. This is not behaviour characteristic of strong coupling, as evident from the discussion of section 6 (figures 16, 17). It is however typical of intermediate–weak-coupling interactions, theoretical consideration of which thus requires specification of bare model parameters. In the following we consider specifically $U/t_* = 1.65$ and $V^2/t_*^2 = 0.2$: these values should not of course be
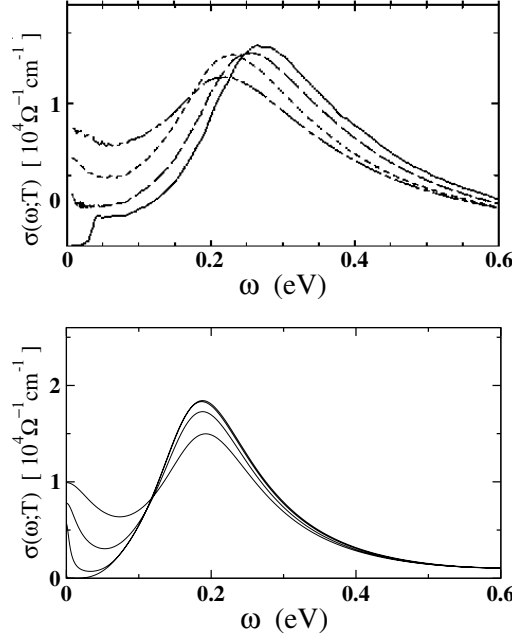
Figure 23. YbB$_{12}$ optical conductivity $\sigma(\omega; T)$ (in Ω^{-1} cm^{-1}) versus ω (in electron volts), for $T = 20, 78, 160$ and 290 K (in obvious sequence). Top panel: experimental results [54]. Bottom panel: theory (for same parameters as figure 22).

taken too seriously *per se*, but they lead within our approach to behaviour representative of intermediate–weak coupling and should be viewed simply as such.

We find with the latter that the low-temperature transport has as expected the activated form, equation (5.1), with $\Delta_{tr} = b\Delta_g$ and the constant $b = 0.47$ (as opposed to $b = 0.40$ for the HCL in strong coupling). Equating the theoretical Δ_{tr} with the experimental $\Delta_{tr} \simeq 68$ K, and taking $\sigma_0 \simeq 10^5 \, \Omega^{-1}$ cm^{-1}, direct comparison between the T-dependence of the theoretical and experimental $\rho(T)$ values is shown in figure 22; and the agreement with experiment is seen to be rather good across essentially the full temperature range. Does this lead to a consistent description of the optical conductivity? The answer is yes in two senses. First, the theoretical estimate of the optical gap $\Delta_{ind} = 2\Delta_g = (2/b)\Delta_{tr}$ follows directly as $\Delta_{ind} \simeq 290$ K $= 25$ meV using only the experimental transport gap above; which value coincides with Δ_{ind} obtained directly from the optical experiments (a situation analogous to that for SmB$_6$ discussed above). Second, the resultant theoretical optical conductivity is shown in the bottom panel of figure 23. It is seen to accord well qualitatively with the experimental results (top panel), both in terms of its overall ω-dependence and thermal evolution, including the redistribution of spectral weight on energy scales beyond the direct gap, for temperatures up to $T = 290$ K, that merely corresponds to the indirect gap itself. (Improved agreement with experiment could no doubt be obtained by playing with the bare parameters, but would add little new.)

8. Summary

We have developed in this paper a non-perturbative local moment approach to dynamics and transport properties of the symmetric periodic Anderson model, the basic microscopic

model for understanding small-gap Kondo insulator materials [3–7]. Our primary focus has naturally been the strong-coupling, Kondo lattice regime. Here the system is characterized by the low-energy scale Δ_g, which, being exponentially small in strong coupling, leads to a pristine separation between low- and high-energy scales, and hence to 'universal scaling' of dynamics/transport in terms of $\tilde{\omega} = \omega/\Delta_g$ and $\tilde{T} = T/\Delta_g$ alone, with no explicit dependence on bare model parameters. It is this single, indirect gap scale Δ_g that is of paramount importance in controlling the physical properties of the system that we have investigated systematically here, for it determines the single-particle spectral gap, the transport gap for dc conductivity and the optical gap in the dynamical conductivity, all of which are simply proportional to each other. It sets the scale for thermal evolution of single-particle dynamics and dc transport, from the gapped/activated behaviour symptomatic of the low-temperature insulator through to the incoherent single-impurity physics that is found to arise naturally for $\tilde{T} \gg 1$. Likewise, it is Δ_g that sets the thermal scale for 'filling' the optical gap with increasing temperature, the much higher direct gap scale naturally also being apparent in the ω-dependence of the optical conductivity, but in strong coupling being essentially irrelevant as a thermal scale for its evolution.

Notwithstanding the innate simplicity of the PAM itself, and the range of material-specific factors it naturally omits, the present theory also appears to account well for experiments on materials such as $Ce_3Bi_4Pt_3$, SmB_6 and YbB_{12}; with many characteristic features arising theoretically apparent in experiment, and a mutually consistent picture of dc transport and optics arising. We believe this lends further support to the essential veracity of both the underlying model (the PAM within DMFT) as well as the present theory, the LMA. Further development of the LMA to encompass the asymmetric PAM, and hence heavy-fermion metals, will be reported in subsequent work.

Acknowledgments

Appendix

Here we sketch the steps leading to equation (5.8) for the leading high-$\tilde{T}$ behaviour of $\rho'_{BL}(T)$ for the BL. Using equation (3.7b) for $\omega = 0$, together with $\langle D_c(\epsilon; \omega)\rangle_\epsilon = D^c(\omega)$ (the c-electron spectrum), $F_{BL}(0; T)$ is given generally by

$$F_{BL}(0; T) = t_*^2 \int_{-\infty}^{\infty} d\omega \; -\frac{\partial f(\omega; T)}{\partial \omega} [D^c(\omega)]^2. \tag{A.1}$$

For the BL, the Feenberg self-energy $S(\omega) = \frac{1}{4}t_*^2 G^c(\omega)$; so equation (2.5a) implies

$$G^c(\omega) = [\gamma(\omega) - \tfrac{1}{4}t_*^2 G^c(\omega)]^{-1} \tag{A.2}$$

which determines the γ-dependence of $G^c \equiv G^c[\gamma]$. For $\tilde{T} \gg 1$ in the scaling regime, $|\gamma| \ll t_*$, which corresponds physically to scattering rates $(\tilde{\gamma}_I(\omega) = \pi\rho_0\gamma_I(\omega) \equiv \tilde{\tau}^{-1}(\omega; T)) \ll 1$ for (all) finite $|\tilde{\omega}|$. Using equation (A.2), the leading asymptotics of $D^c(\omega) = -\frac{1}{\pi} \operatorname{Im} G^c(\omega)$ is given for $|\tilde{\gamma}| \ll 1$ by

$$D^c(\omega) \sim \rho_0 \left[1 - \frac{\pi}{2}\rho_0\gamma_I(\omega) + \mathcal{O}(\tilde{\gamma}_I^2) \right] = \rho_0 \left[1 - \frac{1}{2}\tilde{\tau}^{-1}(\omega; T) + \mathcal{O}(\tilde{\tau}^{-2}) \right] \tag{A.3}$$

whence from equation (A.1)

$$F_{BL}(0; T) \sim [\rho_0 t_*]^2 \left\{ 1 + \int_{-\infty}^{\infty} d\omega \, \frac{\partial f(\omega; T)}{\partial \omega} \tilde{\tau}^{-1}(\omega; T) \right\}. \tag{A.4}$$

Equations (5.6) and (5.7) for $\tilde{\tau}^{-1}(\omega; T)$ then lead to

$$F_{BL}(0; T) \sim [\rho_0 t_*]^2 \left\{ 1 + \frac{3\pi^2}{16 \ln^2(\tilde{T})} \int_{-\infty}^{\infty} dy \, \frac{\partial f(y)}{\partial y} \frac{1}{L(y; \tilde{T})} \right\} \tag{A.5}$$

where $f(y) = [e^y + 1]^{-1}$; and using $L(y; \tilde{T}) \to 1$ as $\tilde{T} \to \infty$ (section 5) gives $F_{BL}(0; T) \sim [\rho_0 t_*]^2 \{1 - \frac{3\pi^2}{16 \ln^2(\tilde{T})}\}$. Using this in equation (5.4) for $\rho'_{BL}(T)$ (together with $[\rho_0 t_*]^2 = \frac{4}{\pi^2}$) gives directly the leading large-$\tilde{T}$ behaviour

$$\rho'_{BL}(T) \overset{\tilde{T} \gg 1}{\sim} \frac{3\pi^2}{16 \ln^2(\tilde{T})} \tag{A.6}$$

as sought.

References

[1] Grewe N and Steglich F 1991 *Handbook on the Physics and Chemistry of Rare Earths* vol 14,
        ed K A Gschneider Jr and L L Eyring (Amsterdam: Elsevier) p 343
[2] Hewson A C 1993 *The Kondo Problem to Heavy Fermions* (Cambridge: Cambridge University Press)
[3] Aeppli G and Fisk Z 1992 *Comments Condens. Matter Phys.* **16** 155
[4] Fisk Z *et al* 1996 *Physica* B **223/224** 409
[5] Takabatake T *et al* 1998 *J. Magn. Magn. Mater.* **177–181** 277
[6] Degiorgi L 1999 *Rev. Mod. Phys.* **71** 687
[7] Riseborough P S 2000 *Adv. Phys.* **49** 257
[8] Vollhardt D 1993 *Correlated Electron Systems* vol 9, ed V J Emery (Singapore: World Scientific)
[9] Pruschke T, Jarrell M and Freericks J K 1995 *Adv. Phys.* **44** 187
[10] Georges A, Kotliar G, Krauth W and Rozenberg M 1996 *Rev. Mod. Phys.* **68** 13
[11] Gebhard F 1997 *The Mott Metal–Insulator Transition (Springer Tracts in Modern Physics)* vol 137 (Berlin:
        Springer)
[12] Shimizu Y and Sakai O 1995 *Computational Physics as a New Frontier in Condensed Matter Research*
        ed H Takayama *et al* (Tokyo: The Physical Society of Japan) p 42
[13] Pruschke T, Bulla R and Jarrell M 2000 *Phys. Rev.* B **61** 12799
[14] Jarrell M, Akhlaghpour H and Pruschke T 1993 *Phys. Rev. Lett.* **70** 1670
[15] Jarrell M 1995 *Phys. Rev.* B **51** 7429
[16] Tahvildar-Zadeh A N, Jarrell M and Freericks J K 1997 *Phys. Rev.* B **55** R3332
        Tahvildar-Zadeh A N, Jarrell M and Freericks J K 1998 *Phys. Rev. Lett.* **80** 5168
[17] Tahvildar-Zadeh A N, Jarrell M, Pruschke T and Freericks J K 1999 *Phys. Rev.* B **60** 10782
[18] Rozenberg M J 1995 *Phys. Rev.* B **52** 7369
[19] Schweitzer H and Czycholl G 1989 *Solid State Commun.* **69** 179
[20] Schweitzer H and Czycholl G 1991 *Phys. Rev. Lett.* **67** 3724
[21] Rozenberg M J, Kotliar G and Kajueter H 1996 *Phys. Rev.* B **54** 8452
[22] Vidhyadhiraja N S, Tahvildar-Zadeh A N, Jarrell M and Krishnamurthy H R 2000 *Europhys. Lett.* **49** 459
[23] Grewe N, Pruschke T and Keiter H 1988 *Z. Phys.* B **71** 75
[24] Pruschke T and Grewe N 1989 *Z. Phys.* B **74** 439
[25] Cox D L and Grewe N 1988 *Z. Phys.* B **71** 321
[26] Newns D M and Read N 1987 *Adv. Phys.* **36** 799
[27] Sun S J, Yang M F and Hong T M 1993 *Phys. Rev.* B **48** 16127
[28] Rice T M and Ueda K 1986 *Phys. Rev.* B **34** 6420
[29] Fazekas P and Brandow B H 1987 *Phys. Scr.* **36** 809
        Fazekas P 1987 *J. Magn. Magn. Mater.* **63/64** 545
[30] Logan D E, Eastwood M P and Tusch M A 1998 *J. Phys.: Condens. Matter* **10** 2673
        Glossop M T and Logan D E 2002 *J. Phys.: Condens. Matter* **14** 6737
[31] Dickens N L and Logan D E 2001 *J. Phys.: Condens. Matter* **13** 4505

[32] Logan D E and Dickens N L 2002 *J. Phys.: Condens. Matter* **14** 3605
[33] Logan D E and Glossop M T 2000 *J. Phys.: Condens. Matter* **12** 985
     Glossop M T and Logan D E 2003 *Europhys. Lett.* **61** 810
[34] Bulla R, Glossop M T, Logan D E and Pruschke T 2000 *J. Phys.: Condens. Matter* **12** 4899
[35] Logan D E and Dickens N L 2001 *Europhys. Lett.* **54** 227
     Logan D E and Dickens N L 2001 *J. Phys.: Condens. Matter* **13** 9713
[36] Smith V E, Logan D E and Krishnamurthy H R 2003 *Eur. Phys. J.* B **32** 49
     (Smith V E, Logan D E and Krishnamurthy H R 2003 *Preprint* cond-mat/0303229)
[37] Feenberg E 1948 *Phys. Rev.* **74** 206
[38] Economou E N 1983 *Green's Functions in Quantum Mechanics* (Berlin: Springer)
[39] Wachter P 1994 *Handbook on the Physics and Chemistry of Rare Earths* vol 19, ed K A Gschneider and
     L L Eyring (Amsterdam: Elsevier) p 177
[40] Logan D E, Eastwood M P and Tusch M A 1997 *J. Phys.: Condens. Matter* **9** 4211
[41] Khurana A 1990 *Phys. Rev. Lett.* **64** 1990
[42] Abrikosov A A 1965 *Physics* **2** 5
[43] Costi T A, Hewson A C and Zlatić V 1994 *J. Phys.: Condens. Matter* **6** 2519
[44] Hamann D R 1967 *Phys. Rev.* **158** 570
[45] Mutou T and Hirashima D S 1994 *J. Phys. Soc. Japan* **63** 4475
[46] Hundley M F, Canfield P C, Thompson J D, Fisk Z and Lawrence J M 1990 *Phys. Rev.* B **42** 6842
[47] Bucher B, Schlesinger Z, Canfield P C and Fisk Z 1994 *Phys. Rev. Lett.* **72** 522
[48] Rasul J W 1997 *Phys. Rev.* B **56** 13701
[49] Nickerson J C, White R M, Lee K N, Bachmann R, Geballe T H and Hull G W Jr 1971 *Phys. Rev.* B **3** 2030
     Allen J W, Batlogg B and Wachter P 1979 *Phys. Rev.* B **20** 4807
[50] Gorshunov B, Sluchanko N, Volkov A, Dressel M, Knebel G, Loidl A and Kunii S 1999 *Phys. Rev.* B **59** 1808
[51] Nanba T, Ohta H, Motokawa M, Kimura S, Kunii S and Kasuya T 1993 *Physica* B **186–188** 440
[52] Travaglini G and Wachter P 1984 *Phys. Rev.* B **29** 893
[53] Iga F, Shimizu N and Takabatake T 1998 *J. Magn. Magn. Mater.* **177–181** 337
[54] Okamura H, Kimura S, Shinozaki H, Nanba T, Iga F, Shimizu N and Takabatake T 1998 *Phys. Rev.* B **58** R7496